ELSEVIER

International Journal of Solids and Structures 41 (2004) 41–67

INTERNATIONAL JOURNAL OF SOLIDS and STRUCTURES

www.elsevier.com/locate/ijsolstr

Coupled chemo-mechanical deterioration of cementitious materials Part II: Numerical methods and simulations

Detlef Kuhl *, Falko Bangert, Günther Meschke

Institute for Structural Mechanics, Ruhr University Bochum, Universitätsstr. 150 IA6-28, 44780 Bochum, Germany

Received 9 July 2003; received in revised form 7 August 2003

Abstract

The paper is concerned with numerical solution procedures for coupled chemo-mechanical simulations of concrete structures subjected to calcium leaching and mechanical damage. The analyses are based upon the chemo-mechanical damage model for cementitious materials presented in the first part of the paper [Int. J. Solids Struct., in press]. These analyses are characterized by a non-linear transient two-field problem described by the displacement field, the pore fluid calcium concentration field and its rate as state variables. The related non-linear first order initial boundary value problem is solved numerically by a semi-discretization strategy. For the temporal discretization the second order accurate implicit generalized mid-point rule is used. The spatial discretization is based upon hierarchical finite elements. The non-linear algebraic system of equations is solved by consistent linearization and Newton–Raphson iteration. Representative simulations of calcium leaching and the coupled chemo-mechanical degradation of concrete structures are presented. In particular, the process of calcium leaching is studied in detail by means of a one-dimensional model problem. Chemo-mechanical interactions on the structural level are investigated in the numerical simulation of a concrete beam subjected simultaneously to mechanical loads and deionized water. It is demonstrated that chemical damage not only reduces the limit load and the stiffness of concrete structures but also their structural behavior.

Keywords: Coupled chemo-mechanical damage; *p*-Finite element method; Implicit time integration; Consistent linearization; Structural failure; Concrete structures

1. Introduction

Long-term degradation of concrete structures under permanently humid environmental conditions is mainly controlled by interacting chemical and mechanical processes leading to the destruction of the micro-structure by the dissolution of cement constituents and the propagation of micro-cracks. In the end, the

* Corresponding author. Tel.: +49-2343229055; fax: +49-2343214149.

E-mail addresses: detlef.kuhl@ruhr-uni-bochum.de (D. Kuhl), falko.bangert@ruhr-uni-bochum.de (F. Bangert), guenther.meschke@ruhr-uni-bochum.de (G. Meschke).

0020-7683/$ - see front matter © 2003 Elsevier Ltd. All rights reserved.
doi:10.1016/j.ijsolstr.2003.08.004

structural collapse may be caused by the superposition of both deterioration mechanisms, even if each individual process is not critical for the safety of the concrete structure. A extensive review of experiments on calcium leaching and interacting chemical and mechanical deterioration processes of cementitious materials and concrete structures, respectively, has been recently given by Kuhl et al. (in press). The following observations have been made in experimental investigations of cement and concrete specimens (see e.g. Adenot and Buil, 1992; Berner, 1988; Delagrave et al., 1997; Gérard, 1996, 2000; Carde et al., 1997, 1996; Carde and François, 1997; Heukamp et al., 2001) and concrete structures (Le Bellégo et al., 2000, 2001a, 2003), respectively:

(1) Calcium leaching is a diffusion controlled process leading to the dissolution of portlandite and ettringite and to the decalcification of CSH-phases.
(2) As a result of the dissolution of calcium two fronts associated with the dissolution of portlandite and CSH can be observed.
(3) Calcium leaching reduces the stiffness and strength and increases the conductivity of cementitious materials.
(4) Mechanical damage accelerates the chemical degradation of concrete as a consequence of improved transport properties.

The present paper is concerned with the computational aspects of a recently developed coupled chemo-mechanical damage model for cementitious materials (Kuhl et al., in press) and the numerical analysis of chemo-mechanical degradation on a structural level. In particular, the ingredients of a multifield finite element formulation, characterized by implicit time integration, consistent linearization, a higher order hierarchical finite element discretization and an iterative Newton–Raphson scheme, are presented. In the chemo-mechanical model, cementitious materials are represented as porous media composed by the connected pore space and the cementitious skeleton. The coupled chemo-mechanical processes are governed by the mass balance of calcium ions within the pore fluid and the balance of linear momentum of the skeleton. Related constitutive models are developed using the theory of mixtures (Bowen, 1976) and the total porosity defined in terms of the initial porosity, the chemically induced porosity and the apparent porosity due to mechanically induced damage. The evolution of chemically and mechanically induced porosities is controlled by internal variables using phenomenological equilibrium chemistry by Gérard (1996, 2000) and Delagrave et al. (1997) and the scalar mechanical damage model by Simo and Ju (1987).

The paper is organized as follows: In the first part, the numerical solution procedures for coupled chemo-mechanical finite element analyses, namely, the weak formulation, the time integration, the linearization, the spatial discretization and the iterative solution technique, are described. In the second part, this finite element model is applied to one-dimensional studies of calcium leaching and to long-term analyses of the coupled chemo-mechanical deterioration of a concrete beam to provide a deeper insight into the interacting degradation processes due to calcium leaching and load induced damage. The numerical examples demonstrate that the chemo-mechanical damage model (Kuhl et al., in press) together with the numerical methods proposed in the present paper are able to reproduce respective experimental results.

2. Numerical solution of the coupled initial boundary value problem

The coupled chemo-mechanical degradation of reactive porous materials due to calcium leaching and mechanically induced damage as described by the chemo-mechanical model presented in the first part of the paper (Kuhl et al., in press), constitutes a non-linear multiple field initial boundary value problem. This coupled problem is defined in terms of the calcium concentration field of the pore fluid $c(\boldsymbol{X})$, its rate $\dot{c}(\boldsymbol{X})$

and the displacement field of the porous material $\boldsymbol{u}(\boldsymbol{X})$. Both fields are coupled through the total porosity, which controls the conductivity, the stiffness and the strength of the porous material. Vice versa, the total porosity depends on the mechanically and chemically induced damage. The coupled system is solved numerically by methods so far employed in the context of non-linear transient problems of structural mechanics (see e.g. Belytschko et al., 2000; Crisfield, 1991, 1997; Zienkiewicz and Taylor, 2000). The following strategy is applied to obtain a step-wise iterative solution of the coupled algebraic system:

(1) Weak formulation of the balances of calcium mass and linear momentum including the related constitutive laws and Neumann boundary conditions.
(2) Time discretization of the weak form and integration by means of the second order accurate implicit generalized mid-point rule, resulting in the semi-discrete weak form.
(3) Consistent linearization of the semi-discrete weak form resulting in the linearized semi-discrete weak form.
(4) Spatial discretization of the non-linear and the linearized semi-discrete weak form by hierarchically generated higher order p-finite elements resulting in the generalized vector of internal forces and the generalized tangent stiffness matrix.
(5) Incremental iterative solution of the resulting system of equations using the iterative Newton–Raphson scheme.

It is worth to notice that changes of the above sequence (2)–(4) do not influence the result of the procedure. The proposed sequence is used to obtain a consistent and compact description of the numerical solution procedure.

2.1. Weak form

The weak form of the coupled initial boundary problem, defined by the calcium mass balance and the balance of momentum

$$\operatorname{div}\boldsymbol{q} + [[\phi_0 + \phi_c]c]^{\cdot} + \dot{s} = 0 \qquad \operatorname{div}\boldsymbol{\sigma} = 0 \tag{1}$$

and the related Neumann boundary conditions and constitutive laws (compare Kuhl et al., in press), is obtained by multiplying Eqs. (1) with appropriate test functions δc and $\delta\boldsymbol{u}$, integration over the domain Ω and the boundaries Γ_q, Γ_σ, respectively, and the re-arrangement by means of the divergence theorem. For a simpler presentation, the resulting virtual work δW is decomposed into the chemical and the mechanical virtual work δW_{c} and δW_{m}, respectively. Both parts are vanishing for chemical and mechanical equilibrium states.

$$\begin{aligned}
&\delta W = \delta W_{\mathrm{c}} + \delta W_{\mathrm{m}} = 0 \\
&\delta W_{\mathrm{c}} = \int_\Omega \delta\boldsymbol{\gamma}\cdot\boldsymbol{q}\,\mathrm{d}V + \int_\Omega \delta c[[\phi_0+\phi_c]\dot{c} + \dot{\phi}_c c + \dot{s}]\,\mathrm{d}V + \int_{\Gamma_q} \delta c\, q^{\star}\,\mathrm{d}A = 0 \\
&\delta W_{\mathrm{m}} = \int_\Omega \delta\boldsymbol{\varepsilon} : \boldsymbol{\sigma}\,\mathrm{d}V - \int_{\Gamma_\sigma} \delta\boldsymbol{u}\cdot\boldsymbol{t}^{\star}\,\mathrm{d}A = 0
\end{aligned} \tag{2}$$

In Eq. (2), $\delta\boldsymbol{\varepsilon} = \nabla^{\mathrm{sym}}\delta\boldsymbol{u}$ and $\delta\boldsymbol{\gamma} = -\nabla\delta c$.

2.2. Time integration by the generalized mid-point rule

In order to integrate the considered initial value problem, the generalized mid-point rule by Chung and Hulbert (1993) based on the classical time approximation by Newmark (1959) is applied. The

advantages of the chosen time integration scheme are its implicit formulation, its second order accuracy, its simple extension to second order differential equations and the applicability of classical error indicators and adaptive time stepping schemes in the linear and non-linear regime (see e.g. Zienkiewicz and Xie, 1991; Kuhl and Ramm, 1999). As the basis for the integration, the time interval of interest $[0, T_i]$ is partitioned into time intervals $[t_n, t_{n+1}]$ with corresponding time steps $\Delta t = t_{n+1} - t_n$. Assuming known state variables $\boldsymbol{u}_n, c_n$ and $\dot{c}_n$ at time t_n and prescribed Neumann boundary conditions $\boldsymbol{t}^\star(t)$ and $q^\star(t)$ for all $t \in [0, T_i]$, the time integration requires the successive determination of the state variables $\boldsymbol{u}_{n+1}$, c_{n+1} and $\dot{c}_{n+1}$ at the end of each time step. Using the Newmark approximation (Newmark, 1959) and the related time integration parameters γ and β to calculate the rate of the calcium concentration of the pore fluid at time t_{n+1},

$$\dot{c}_{n+1}(c_{n+1}) = \frac{\gamma}{\beta \Delta t}[c_{n+1} - c_n] - \frac{\gamma - \beta}{\beta}\dot{c}_n \tag{3}$$

the set of variables is reduced to the displacements $\boldsymbol{u}_{n+1}$ and the concentration c_{n+1} at the end of the time step. Furthermore, the definition of generalized mid-point state variables $\boldsymbol{u}_{n+1-\alpha}$, $c_{n+1-\alpha}$ and $\dot{c}_{n+1-\alpha}$ with $0 \leqslant \alpha \leqslant 1$ is introduced according to Chung and Hulbert (1993):

$$\begin{aligned} \boldsymbol{u}_{n+1-\alpha} &= [1-\alpha]\boldsymbol{u}_{n+1} + \alpha \boldsymbol{u}_n \\ c_{n+1-\alpha} &= [1-\alpha]c_{n+1} + \alpha c_n \\ \dot{c}_{n+1-\alpha} &= [1-\alpha]\dot{c}_{n+1} + \alpha \dot{c}_n \end{aligned} \tag{4}$$

The weak form (2) evaluated at the generalized mid-point $n+1-\alpha$, representing the time $t_{n+1-\alpha} = [1-\alpha]t_{n+1} + \alpha t_n$, yields the semi-discrete form of the coupled chemo-mechanical problem:

$$\begin{aligned} \delta W_{n+1-\alpha} &= \int_\Omega \delta \boldsymbol{\gamma}_{n+1-\alpha} \cdot \boldsymbol{q}_{n+1-\alpha} \, \mathrm{d}V + \int_{\Gamma_q} \delta c_{n+1-\alpha} \, q^\star_{n+1-\alpha} \, \mathrm{d}A + \int_\Omega \delta c_{n+1-\alpha} [[\phi_0 + \phi_c]\dot{\boldsymbol{c}} + \dot{\phi}_c c + \dot{s}]_{n+1-\alpha} \, \mathrm{d}V \\ &\quad + \int_\Omega \delta \boldsymbol{\varepsilon}_{n+1-\alpha} : \boldsymbol{\sigma}_{n+1-\alpha} \, \mathrm{d}V - \int_{\Gamma_\sigma} \delta \boldsymbol{u}_{n+1-\alpha} \cdot \boldsymbol{t}^\star_{n+1-\alpha} \, \mathrm{d}A \\ &= 0 \end{aligned} \tag{5}$$

The indices $(\cdot)_{n+1-\alpha}$ of non-state variables $(\cdot)$ indicate that the related value $(\cdot)$ is evaluated based upon the state variables $c_{n+1-\alpha}$ and $\boldsymbol{u}_{n+1-\alpha}$ at time $t_{n+1-\alpha}$. The time discrete Neumann boundary conditions are calculated according to Eq. (4):

$$q^\star_{n+1-\alpha} = [1-\alpha]q^\star_{n+1} + \alpha q^\star_n, \qquad \boldsymbol{t}^\star_{n+1-\alpha} = [1-\alpha]\boldsymbol{t}^\star_{n+1} + \alpha \boldsymbol{t}^\star_n \tag{6}$$

2.3. Consistent linearization of the semi-discrete weak form

Linearization of Eq. (5) with respect to the concentration c_{n+1} and the displacement vector $\boldsymbol{u}_{n+1}$ at the end of the time interval $[t_n, t_{n+1}]$ leads to the linearized semi-discrete weak form of the chemo-mechanical set of equations:

$$
\begin{aligned}
\Delta\delta W_{n+1-\alpha} = & \int_\Omega \delta\boldsymbol{\gamma}_{n+1-\alpha} \cdot \left[\frac{\partial \boldsymbol{q}}{\partial \boldsymbol{\varepsilon}}\right]_{n+1-\alpha} \frac{\partial \boldsymbol{u}_{n+1-\alpha}}{\partial \boldsymbol{u}_{n+1}} : \Delta\boldsymbol{\varepsilon}_{n+1}\,\mathrm{d}V \\
& + \int_\Omega \delta\boldsymbol{\gamma}_{n+1-\alpha} \cdot \left[\frac{\partial \boldsymbol{q}}{\partial c}\right]_{n+1-\alpha} \frac{\partial c_{n+1-\alpha}}{\partial c_{n+1}} \Delta c_{n+1}\,\mathrm{d}V \\
& + \int_\Omega \delta c_{n+1-\alpha} \left[\frac{\partial s}{\partial c}\right]_{n+1-\alpha} 2\frac{\partial \phi_c}{\partial s} \dot{c}_{n+1-\alpha} \frac{\partial c_{n+1-\alpha}}{\partial c_{n+1}} \Delta c_{n+1}\,\mathrm{d}V \\
& + \int_\Omega \delta c_{n+1-\alpha} \left[\frac{\partial^2 s}{\partial \kappa_c^2}\right]_{n+1-\alpha} \phi_s \frac{\partial \kappa_c}{\partial c} \dot{c}_{n+1-\alpha} \frac{\partial c_{n+1-\alpha}}{\partial c_{n+1}} \Delta c_{n+1}\,\mathrm{d}V \\
& + \int_\Omega \delta c_{n+1-\alpha} \left[\frac{\partial s}{\partial c}\right]_{n+1-\alpha} \phi_s \frac{\partial \dot{c}_{n+1-\alpha}}{\partial \dot{c}_{n+1}} \frac{\partial \dot{c}_{n+1}}{\partial c_{n+1}} \Delta c_{n+1}\,\mathrm{d}V \\
& + \int_\Omega \delta c_{n+1-\alpha} [\phi_0 + \phi_{cn+1-\alpha}] \frac{\partial \dot{c}_{n+1-\alpha}}{\partial \dot{c}_{n+1}} \frac{\partial \dot{c}_{n+1}}{\partial c_{n+1}} \Delta c_{n+1}\,\mathrm{d}V \\
& + \int_\Omega \delta\boldsymbol{\varepsilon}_{n+1-\alpha} : \left[\frac{\partial \boldsymbol{\sigma}}{\partial \boldsymbol{\varepsilon}}\right]_{n+1-\alpha} \frac{\partial \boldsymbol{u}_{n+1-\alpha}}{\partial \boldsymbol{u}_{n+1}} : \Delta\boldsymbol{\varepsilon}_{n+1}\,\mathrm{d}V \\
& + \int_\Omega \delta\boldsymbol{\varepsilon}_{n+1-\alpha} : \left[\frac{\partial \boldsymbol{\sigma}}{\partial c}\right]_{n+1-\alpha} \frac{\partial c_{n+1-\alpha}}{\partial c_{n+1}} \Delta c_{n+1}\,\mathrm{d}V
\end{aligned} \tag{7}
$$

Herein, the abbreviation

$$
\phi_s = \left[1 + \frac{\partial \phi_c}{\partial s} c_{n+1-\alpha}\right] \tag{8}
$$

and derivatives considering the time integration scheme are incorporated. κ_c is the threshold value of the calcium concentration within the pore fluid associated with chemical equilibrium between calcium bounded within the skeleton and solved within the pore fluid. For the employed generalized mid-point rule and the Newmark time approximations the derivatives associated with the temporal approximations are obtained from Eqs. (3) and (4):

$$
\begin{aligned}
& \frac{\partial \dot{c}_{n+1}}{\partial c_{n+1}} = \frac{\gamma}{\beta \Delta t} \\
& \frac{\partial \boldsymbol{u}_{n+1-\alpha}}{\partial \boldsymbol{u}_{n+1}} = \frac{\partial c_{n+1-\alpha}}{\partial c_{n+1}} = \frac{\partial \dot{c}_{n+1-\alpha}}{\partial \dot{c}_{n+1}} = 1 - \alpha
\end{aligned} \tag{9}
$$

Further derivatives $\partial s/\partial c = \partial s/\partial \kappa_c\, \partial \kappa_c/\partial c$, $\partial \phi_c/\partial s$, $\partial s/\partial \kappa_c$, $\partial^2 s/\partial \kappa_c^2$ and $\partial \kappa_c/\partial c$ contained in Eq. (7) are summarized in the first part of the present paper (Kuhl et al., in press).

2.4. Finite element discretization using p-finite elements

The finite element discretization of the virtual work in the original and linearized form is performed by a family of isoparametric hierarchically generated *p*-finite elements based on Legendre polynomials (see e.g. Szabó and Babuška, 1992; Schwab, 1998). As demonstrated by Bangert (1999), this family of elements permits different orders of approximation for the concentration and deformation fields in addition to an effective coding of higher order multifield elements. Consequently, this hierarchical family of element is well suited for adaptive coupled analyses. Furthermore, higher order approximations avoid the main disadvantage of low order finite elements, namely the locking phenomenon, in a natural manner (see e.g. Düster et al., 2001; Schwab, 1998).

The finite element discretization is based on the subdivision of the investigated domain in element domains $\Omega = \bigcup_{e=1}^{ne} \Omega^e$ and the approximation of the position vector $\boldsymbol{X}$ and the state variables $c, \boldsymbol{u}$ by means of shape functions N^i, given in Appendix A.1, and related nodal values $\boldsymbol{X}^i$, c^i and $\boldsymbol{u}^i$:

$$\boldsymbol{X} \approx \sum_{i=1}^{m} N^i \boldsymbol{X}^i, \qquad c \approx \sum_{i=1}^{m} N^i c^i, \qquad \boldsymbol{u} \approx \sum_{i=1}^{m} N^i \boldsymbol{u}^i \tag{10}$$

For the finite element discretization, the approximations (10), the resulting approximations (A.14) of the virtual concentration gradient $\delta\boldsymbol{\gamma}$ and the specific internal virtual work $\delta\boldsymbol{\varepsilon} : \boldsymbol{\sigma}$, respectively, and the linearization of the specific internal virtual work with respect to the strain and concentration increments (A.16) are used. Application of these approximations to the semi-discrete form (5) and the linearized semi-discrete form (7) and integration over the element domain Ω^e yields the discrete forms on the element level:

$$\begin{aligned}
\delta W^e_{n+1-\alpha} &\approx \sum_{i=1}^{m} \begin{bmatrix} \delta c^i_{n+1-\alpha} \\ \delta \boldsymbol{u}^i_{n+1-\alpha} \end{bmatrix} \cdot \begin{bmatrix} r^i_c + r^i_{ce} \\ \boldsymbol{r}^i_m - \boldsymbol{r}^i_{me} \end{bmatrix}_{n+1-\alpha} = \delta \boldsymbol{d}^e_{n+1-\alpha} \cdot [\boldsymbol{r} - \boldsymbol{r}_e]^e_{n+1-\alpha} \\
\Delta\delta W^e_{n+1-\alpha} &\approx \sum_{i=1}^{m} \sum_{j=1}^{m} \begin{bmatrix} \delta c^i_{n+1-\alpha} \\ \delta \boldsymbol{u}^i_{n+1-\alpha} \end{bmatrix} \cdot \begin{bmatrix} k^{ij}_{cc} \boldsymbol{k}^{ij\mathrm{T}}_{cm} \\ \boldsymbol{k}^{ij}_{mc} \boldsymbol{k}^{ij}_{mm} \end{bmatrix}_{n+1-\alpha} \begin{bmatrix} \Delta c^j_{n+1} \\ \Delta \boldsymbol{u}^j_{n+1} \end{bmatrix} = \delta \boldsymbol{d}^e_{n+1-\alpha} \cdot \mathbf{K}^{te}_{n+1-\alpha} \Delta \boldsymbol{d}^e_{n+1}
\end{aligned} \tag{11}$$

The virtual work is described in terms of the generalized vectors of the internal and external forces $\boldsymbol{r}^e(\boldsymbol{d}^e)$ and $\boldsymbol{r}^e_e$, respectively, defining the generalized residual forces $\boldsymbol{r}^e_e - \boldsymbol{r}^e(\boldsymbol{d}^e)$. The linearized virtual work is formulated using the generalized tangent stiffness matrix $\mathbf{K}^{te}(\boldsymbol{d}^e)$. The element vector $\boldsymbol{d}^e$ contains the element degrees of freedom, namely the nodal values of the concentration c^i and the nodal displacement vectors $\boldsymbol{u}^i$. r^i_c and r^i_{ce} are the nodal values of the internal and external calcium mass flux, $\boldsymbol{r}^i_m$ and $\boldsymbol{r}^i_{me}$ are the internal and equivalent external forces, $\boldsymbol{k}^{ij}_{mm}$ are the mechanical element tangent stiffness tensors associated with nodes i and j, k^{ij}_{cc} are the scalar valued effective conductivities, $\boldsymbol{k}^{ij}_{mc}$ and $\boldsymbol{k}^{ij}_{cm}$ are the first order chemo-mechanical coupling tensors. These vectors and tensors are given in detail by Eqs. (A.15) and (A.17). After assembling of the above element quantities, the vectors containing the degrees of freedom of the concentration and the displacements, the generalized residual forces and the generalized tangent stiffness matrix are obtained on the structural level:

$$\begin{aligned}
\delta W_{n+1-\alpha} &= \sum_{e=1}^{ne} \delta W^e_{n+1-\alpha} & \boldsymbol{d}_{n+1-\alpha} &= \bigcup_{e=1}^{ne} \boldsymbol{d}^e_{n+1-\alpha} \\
\Delta\delta W_{n+1-\alpha} &= \sum_{e=1}^{ne} \Delta\delta W^e_{n+1-\alpha} & \mathbf{K}^t_{n+1-\alpha} &= \bigcup_{e=1}^{ne} \mathbf{K}^{te}_{n+1-\alpha} \\
& & [\boldsymbol{r} - \boldsymbol{r}_e]_{n+1-\alpha} &= \bigcup_{e=1}^{ne} [\boldsymbol{r} - \boldsymbol{r}_e]^e_{n+1-\alpha}
\end{aligned} \tag{12}$$

2.5. Iterative solution using the Newton–Raphson scheme

Approximation of the Taylor expansion of the semi-discrete virtual work (5), using the finite element discretization described in Section 2.4,

$$\delta W^{k+1}_{n+1-\alpha} = \delta W^k_{n+1-\alpha} + \Delta\delta W^k_{n+1-\alpha} \approx \delta \boldsymbol{d}_{n+1-\alpha} \cdot [\boldsymbol{r}(\boldsymbol{d}^k_{n+1}) - \boldsymbol{r}_e]_{n+1-\alpha} + \delta \boldsymbol{d}_{n+1-\alpha} \cdot \mathbf{K}^t_{n+1-\alpha}(\boldsymbol{d}^k_{n+1}) \Delta \boldsymbol{d}_{n+1} \approx 0 \tag{13}$$

leads to the iterative Newton–Raphson scheme

$$\mathbf{K}^t_{n+1-\alpha}(\boldsymbol{d}^k_{n+1}) \Delta \boldsymbol{d}_{n+1} = [\boldsymbol{r}_e - \boldsymbol{r}(\boldsymbol{d}^k_{n+1})]_{n+1-\alpha} \tag{14}$$

Herein, the Newton correction or, equivalently, the incremental solution vector

$$\Delta \boldsymbol{d}_{n+1} = \boldsymbol{d}_{n+1}^{k+1} - \boldsymbol{d}_{n+1}^{k} \tag{15}$$

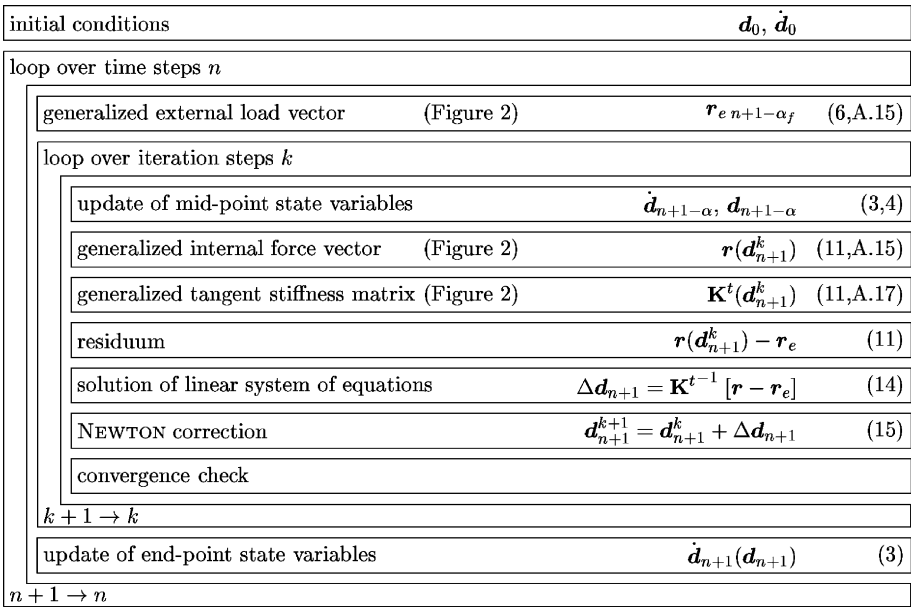

Fig. 1. Algorithmic set-up on the structural level (vector $\boldsymbol{d}$ contains the concentrations $\boldsymbol{c}$ and the displacements $\boldsymbol{u}$).

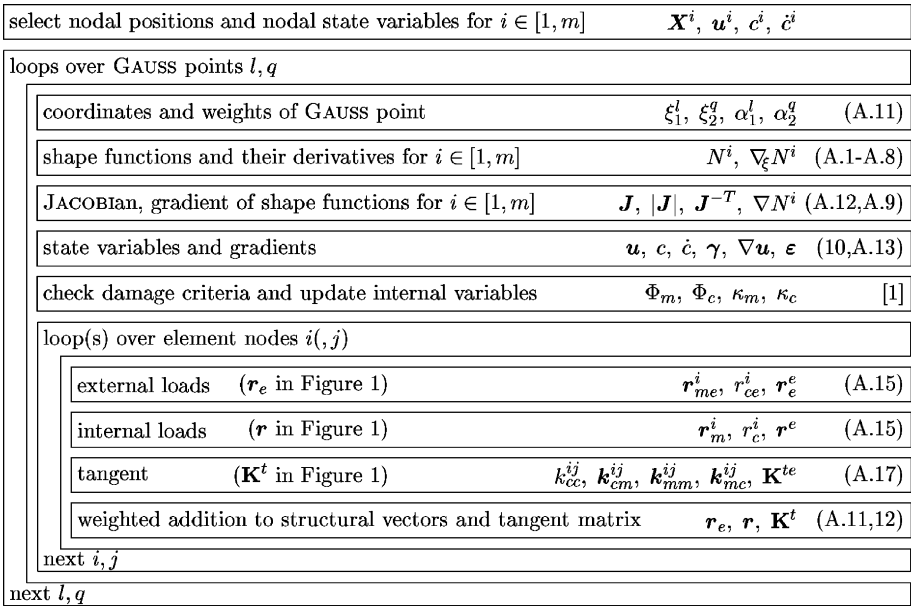

Fig. 2. Algorithmic set-up on the element level. Calculation of the generalized residual forces $\boldsymbol{r}^e - \boldsymbol{r}_e^e$ and $\boldsymbol{r} - \boldsymbol{r}_e$ and the generalized tangent stiffness matrices $\mathbf{K}^{te}$ and $\mathbf{K}^t$.

is defined. After a convergent solution of Eq. (13) is obtained, the calcium concentration rate at the end of the time step is updated by means of Eq. (3). Since concentrations and displacements contained in the solution vector $\boldsymbol{d}_{n+1}$ have different physical units and may also have different dimensions, their convergence should be checked independently.

2.6. Algorithmic set-up

The algorithmic scheme of the numerical solution procedures for the coupled analysis of dissociation–diffusion of calcium and chemo-mechanical damage in cementitious materials on the structural level is illustrated in Fig. 1. Fig. 2 contains the respective algorithmic scheme on the element level.

3. Representative numerical simulations

In this section the proposed chemo-mechanical damage model together with the numerical solution strategy presented in Section 2 is applied to analyses of the one-dimensional reaction–diffusion process within a concrete bar and the coupled chemo-mechanical deterioration of a plane cementitious beam. Material and model parameters for both analyses are given in Table 1.

3.1. One-dimensional calcium leaching

In this subsection numerical and physical aspects of the analysis of the dissolution and transport of calcium within a bar made of cement (Fig. 3) are investigated. The initial condition is characterized by a state of chemical equilibrium of the virgin material $c(t_0) = c_0 \; \forall \boldsymbol{X} \in \Omega$. The concrete bar is subjected to a Dirichlet boundary condition $c^\star(t)$ at the bottom (Γ_c) (see load histories at the right-hand side of Fig. 3). All other surfaces are assumed to be insulated ($q^\star = 0$). Since the boundary conditions are spatially constant on Γ_c, the calcium concentration of the pore fluid c varies only in X_2 direction within the domain Ω. Consequently, only a one-dimensional system needs to be solved for the present studies. However, the bar is discretized by NE two-dimensional finite elements with polynomial degree p. The investigated h- and p-refinements are contained on the left-hand side of Fig. 3. Independent of the chosen spatial discretization 10×10 Gauss-points are used for the integration of the finite element quantities. This high order integration scheme was only used to obtain a high spatial resolution of the variables κ_c, s and $\dot{s}$ for their graphical representation. The computations could be also performed with equivalent accuracy by adapting the number of Gauss-points to the polynomial degree of the finite elements. For the time integration the numerically undamped mid-point rule with the parameters $\alpha = 2\beta = \gamma = 0.5$ and time steps $\Delta t = 275$ d is

Table 1
Material and model parameters

$\lambda_0 = 12.153 \times 10^9$ N/m^2	$c_0 = 20.7378$ mol/m^3	$n = 85$
$\mu_0 = 18.229 \times 10^9$ N/m^2	$c_p = 19$ mol/m^3	$m = 5$
$\phi_0 = 0.2$	$c_{\text{csh}} = 1.5$ mol/m^3	$\frac{M}{\rho} = 3.5 \times 10^{-5}$ m^3/mol
$\kappa_m^0 = 1.1 \times 10^{-4}$	$s_0 = 15$ kmol/m^3	$D_{00} = 791.8 \times 10^{-12}$ m^2/s
$\alpha_m = 0.9$	$s_h = 9$ kmol/m^3	$D_{0c} = 96.85 \times 10^{-12}$ m^2/s $\sqrt{\text{m}^3/\text{mol}}$
$\beta_m = 1000$	$\alpha_c = 0.565$	

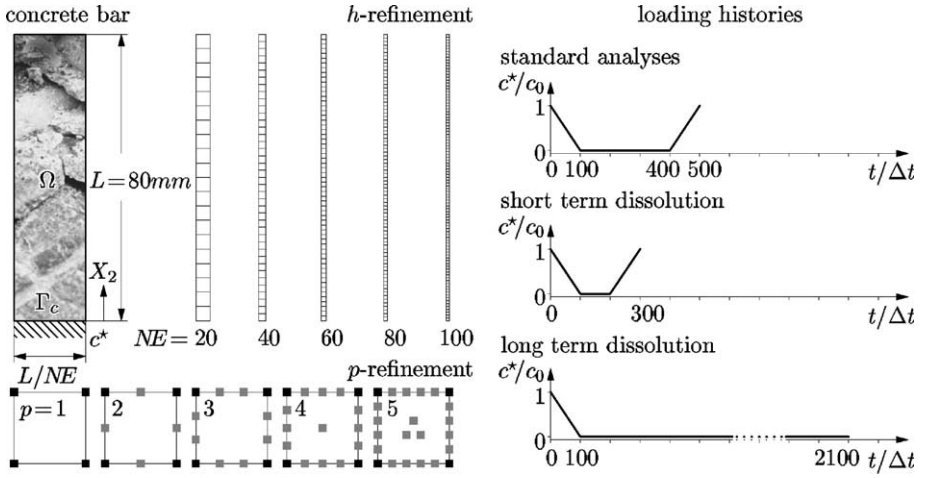

Fig. 3. One-dimensional calcium leaching: geometry, boundary conditions, discretization, h- and p-refinement and loading histories.

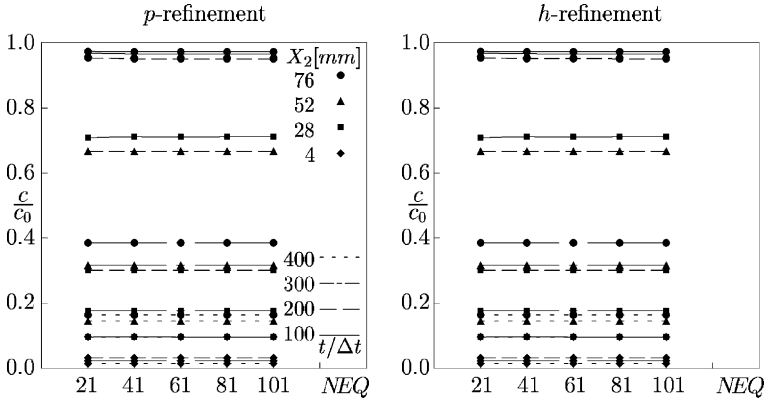

Fig. 4. One-dimensional calcium leaching: convergence of p- and h-refinement for different positions and time steps.

Table 2
One-dimensional calcium leaching: convergence of c/c_0 for the p-refinement

NEQ	$X_2 = 76$ mm	$X_2 = 52$ mm	$X_2 = 28$ mm	$X_2 = 4$ mm	$t/\Delta t$
21	0.97324785898	0.96794311836	0.70815364937	0.09523411596	100
41	0.97224611579	0.96560956321	0.71110716903	0.09556336014	
61	0.97223399541	0.96558011940	0.71057962272	0.09545208749	
81	0.97223315154	0.96557760949	0.71076420594	0.09545460464	
101	0.97223301893	0.96557711281	0.71067375999	0.09544927379	
21	0.16315601703	0.14366744303	0.09464904908	0.01323588327	400
41	0.16305813056	0.14356512504	0.09455423671	0.01321756888	
61	0.16305012586	0.14355677314	0.09454933744	0.01321727474	
81	0.16304967740	0.14355645247	0.09454924341	0.01321678770	
101	0.16304743030	0.14355631986	0.09454921930	0.01321764122	

used. The initial condition for the concentration field is given by the equilibrium concentration of the chemically sound concrete $c_0^\star = c_0$.

3.1.1. h- and p-refinement and convergence

The convergence of finite element analyses of one-dimensional calcium leaching, using alternatively the *h*- and *p*- finite element refinement according to Fig. 3, is illustrated in Fig. 4 and Table 2. The calcium concentration c is calculated at several positions (marked by circular, triangular, square and rhombic points) and different time steps (marked by different line types). NEQ represents the number of degrees of freedom of the equivalent discretization by one-dimensional finite elements. For both refinement strategies the solution is only slightly affected after the first refinement step and approximately constant for further refinements. Hence, already for relatively coarse discretizations accurate finite element solutions are obtained. An additional analysis with NE = 10 and $p = 1$ could not be successfully completed due to lack of convergence during the Newton–Raphson iteration at the beginning of portlandite dissolution. As was

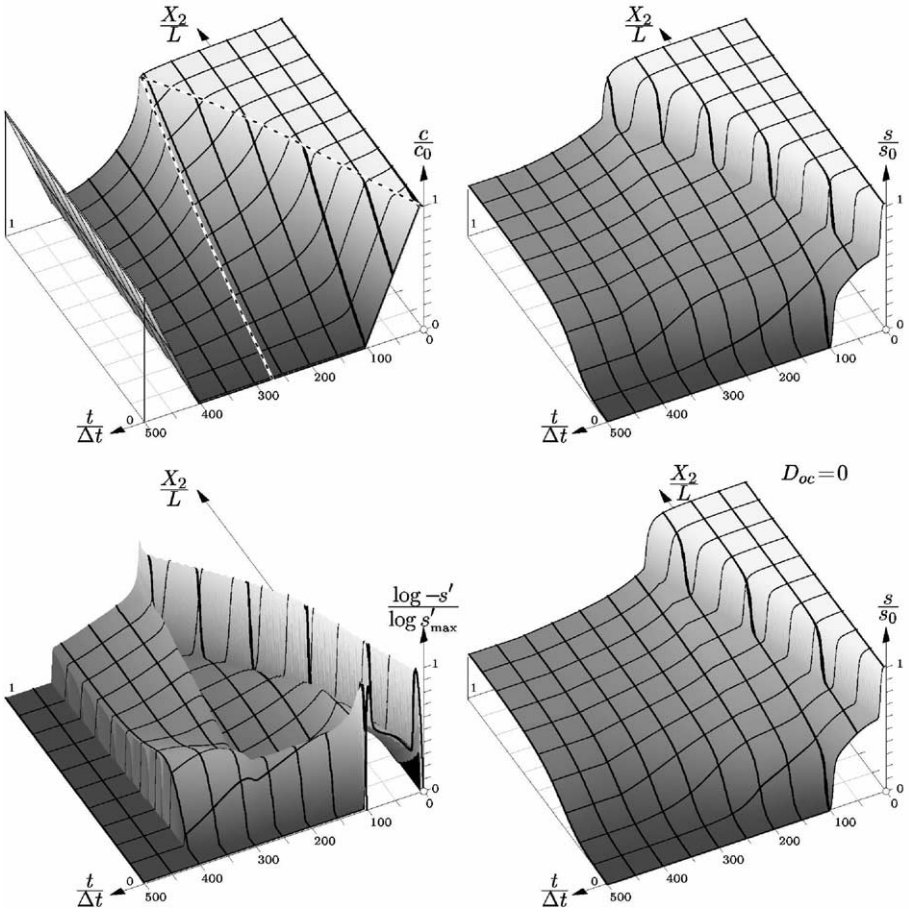

Fig. 5. One-dimensional calcium leaching: variation of the calcium concentration c and s and the calcium mass production s' [mol/m^3] as functions of the position X_2 and the time t using Kohlrausch's law ($D_{0c} \neq 0$) and the standard transport model ($D_{0c} = 0$) (NE = 40, $p = 1$).

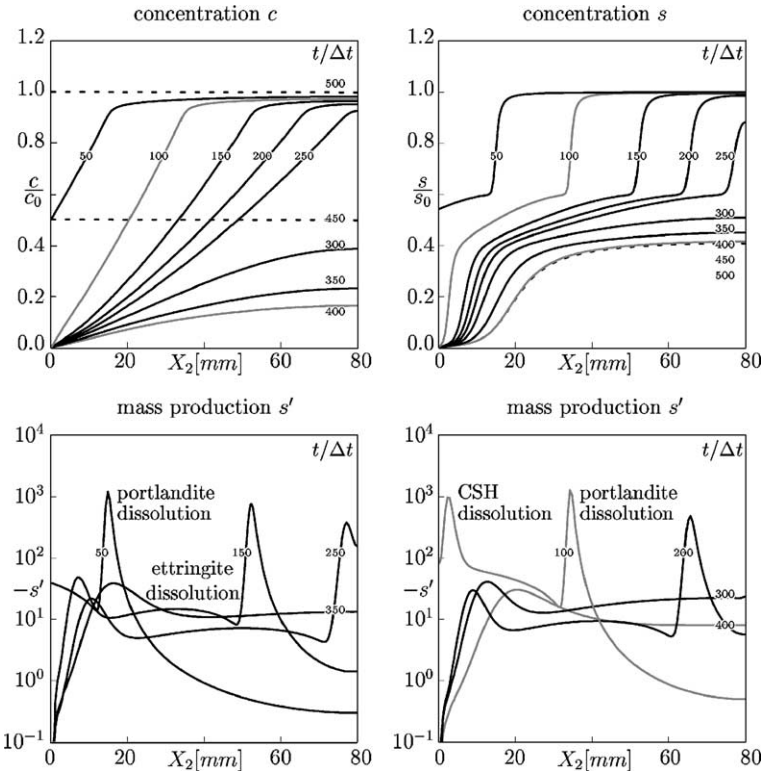

Fig. 6. One-dimensional calcium leaching: profiles of c/c_0, s/s_0 and s' [mol/m^3] using Kohlrausch's law (NE = 20, $p = 5$).

shown by Becker (2001), this lack of convergence occurs independently of the spatial discretization technique. In particular, Becker (2001) has compared the h- and p-finite element method, the finite volume method and the finite difference method. The reason for the failure of the Newton–Raphson iteration is the localization of the cement dissolution zones within small bands of the structure (compare Figs. 5–9), which cannot be resolved by a coarse mesh with low order finite elements, finite volumes or finite difference stars. Such convergence problems may be avoided, if an error controlled adaptive mesh refinement, using a fine discretization in dissolution zones and a coarser mesh elsewhere, is used (see Díez et al., 2002). Alternatively, adaptively controlled higher order finite elements can be applied.

3.1.2. Discussion of calcium dissolution–diffusion

The process of one-dimensional calcium dissolution–diffusion using the chemical model together with Kohlrausch's law as proposed in the first part of the paper (Kuhl et al., in press) is studied by means of finite element discretizations characterized by NE = 40 and $p = 1$ or NE = 20 and $p = 5$. Chemical loading and unloading is applied according to the 'standard' case as illustrated in Fig. 3. Fig. 5 shows the distribution of the primary variable c, namely the calcium concentration of the pore fluid, the calcium concentration of the skeleton s and the mass production due to cement dissolution $s' = \dot{s}\Delta t$ during one time step Δt as functions of the position X_2 within the concrete bar and the time t. It should be noted that s is related to the internal chemical variable κ_c by means of the phenomenological chemistry model proposed by Gérard (1996) and Delagrave et al. (1997). The relation between the calcium concentration s and the chemically induced porosity $\phi_c = \mathscr{M}/\rho[s_0 - s]$ is linear. For the graphical representation of the mass production s' a

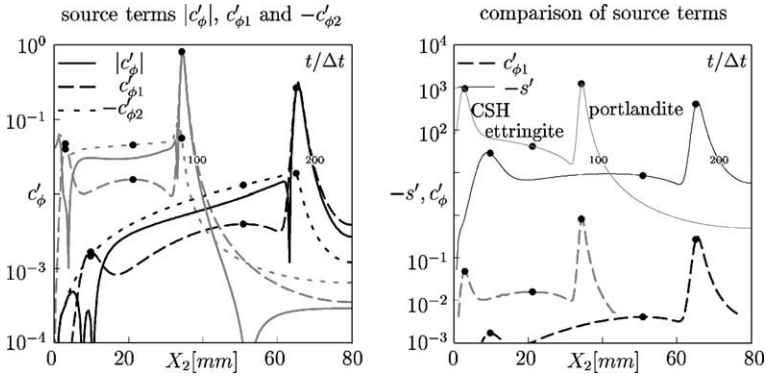

Fig. 7. One-dimensional calcium leaching: dimensional analysis of the source terms $c'_\phi = c'_{\phi 1} + c'_{\phi 2}$ and s', both given in mol/m^3 (NE = 20, $p = 5$).

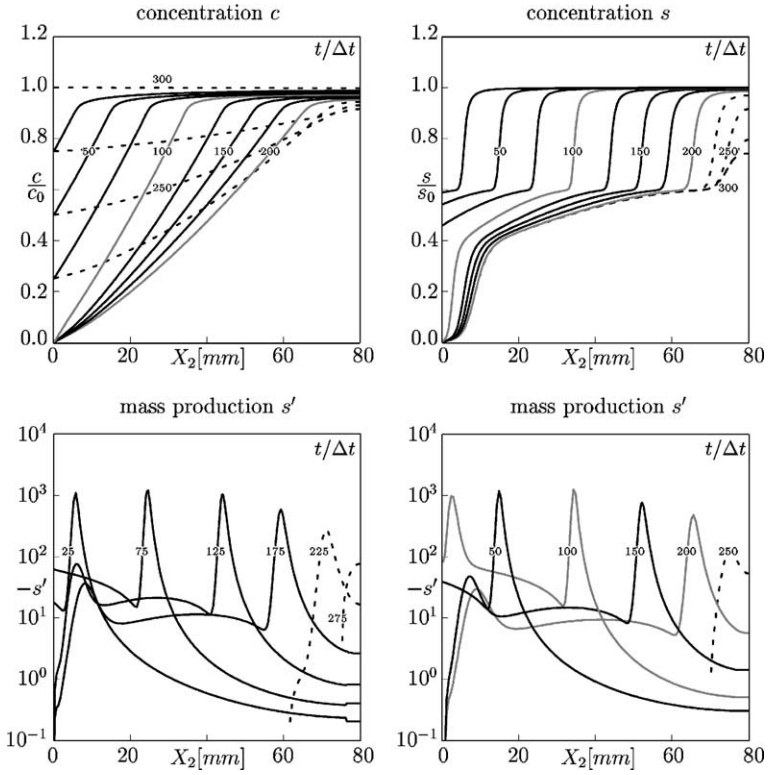

Fig. 8. One-dimensional calcium leaching (short-term dissolution): profiles of c/c_0, s/s_0 and $\dot{s}$ [mol/m^3 d] (NE = 20, $p = 5$).

logarithmic measure $\log -s'$ is used. This allows for the visualization of both the dominant dissolution of portlandite as well as the less pronounced fronts associated with the dissolution of ettringite and CSH-phases, respectively. Values of $-s' < 1$ mol/m^3 are set to $-s' = 1$ mol/m^3 to enable the visualization of the secondary CSH and ettringite dissolution. All plots are given in a dimensionless form by using the bar

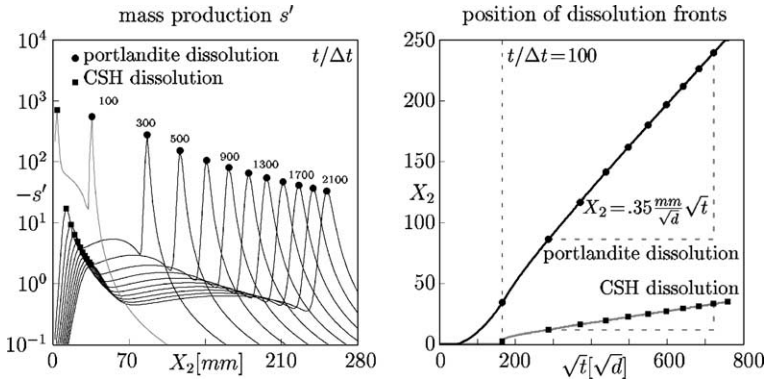

Fig. 9. One-dimensional calcium leaching (long-term dissolution): propagation of portlandite and CSH dissolution fronts, front position X_2 [mm] as function of the square root of time $\sqrt{t}$ [$\sqrt{\text{d}}$].

length L, the time step Δt and the equilibrium concentrations of the sound material c_0 and s_0 to normalize X_2, t, c and s. The mass production s' is normalized with respect to the maximum negative mass production within the considered spatial and temporal domain, calculated as $s'_{\max} = -1295$ mol/m^3. Time history plots are defined by lines $X_2/L = \text{const.}$ and spatial profiles are given by lines $t/\Delta t = \text{const.}$, where the thickness of the lines represents the slope of the functions $(\cdot)(X_2, t)$ normal to the time histories or profiles. For the comparison of higher order transport models accounting for ion–ion interactions due to the electrophoretic and relaxation effects and standard transport models, characterized by $D_{0c} = 0$, the s-plots are included for both models in Fig. 5. Respective plots of the distribution of c/c_0, s/s_0 and s' along the bar axis are contained in Fig. 6. The profiles associated with $t/\Delta t = 100$ and $t/\Delta t = 400$ are identified by gray lines. Profiles corresponding to chemical unloading are marked by dashed lines.

As a consequence of the decreasing concentration $c^\star$ at the boundary Γ_c a concentration gradient $\partial c/\partial X_2$ is introduced within the pore fluid and calcium ions are moving outwards. Consequently, the calcium concentration c within the pore fluid is reduced and the chemical equilibrium between calcium ions in the interstitial pore solution and the calcium bounded in the skeleton is violated. To restore chemical equilibrium, cement-phases are dissociated, which means that the mass production by instantaneous dissolution of the skeleton ($\dot{s} < 0$) is activated and the concentration of calcium in the skeleton s is reduced.

The history plots of the primary variable c in Fig. 5 show that the time scale of the reaction–diffusion system, i.e. the gradient of $c(X_2, t)$ with respect to the time axis, changes three times during the calculation. The first change is associated with the dissolution of portlandite, which affects the chemical porosity ϕ_c and, consequently, the macroscopic conductivity ϕD_0. The second change of the time scale corresponds to the end of the portlandite dissolution as soon as the associated dissolution front reaches the end of the bar ($X_2/L = 1$) at time $t/\Delta t \approx 260$. If no portlandite remains to be solved, the source term $\dot{s} = s'/\Delta t$ of the local calcium mass balance (1) is significantly reduced. Consequently, the temporal variation of the calcium concentration c within the pore fluid is accelerated. This change of the time scale is manifested in Fig. 5 by a kink in the $c(X_2, t)$ graph marked by a dashed line. After chemical unloading is prescribed ($400 < t/\Delta t < 500$), a third change of the time scale will be obtained. In this case the source term $\dot{s}$ is equal to zero and the time dependence of the mass balance (1) is only controlled by the storage term $[[\phi_0 + \phi_c]c]^\cdot$ which is several dimensions smaller than $\dot{s}$ (compare Section 3.1.3). Therefore, as $c^\star(t)$ at the boundary is increased, the concentration c in the whole domain is rapidly increased, with an almost negligible spatial gradient (see the dashed, nearly horizontal lines in Fig. 6 corresponding to chemical unloading). In contrast to the outflow of calcium ions the refilling of the cement sample is much faster. This model behavior during

chemical unloading follows partially from the increasing conductivity D_0 resulting from the increasing pore space created by chemical dissolution and, more importantly, from the irreversible character of the skeleton dissolution, which means, that in the chemical unloading range the source term $\dot{s}$ in Eq. (1) does not exist.

The profiles of the calcium concentration s in the skeleton (Fig. 5) show a pronounced front of the portlandite dissolution within the first 80 time steps. As soon as the concentration c in the pore fluid becomes smaller than the equilibrium concentration of the CSH-phases ($c < c_{\text{csh}}$), a second dissolution front related to the dissolution of portlandite and CSH-phases can be observed. Ettringite is dissolved between these two fronts. While the portlandite front propagates through the cement sample with a nearly unchanged step-like shape, the CSH front moves much slower and its shape is smoothed with time. The different characteristics of the two dissolution mechanisms is reflected in the larger mass production s' per time increment during the dissolution of the portlandite as compared to the CSH dissolution (lower parts of Figs. 5 and 6). From Figs. 5 and 6 it can be observed that the propagation of the portlandite dissolution front is decelerated with increasing advance of the front. This phenomenon results from the increasing distance for the transport of calcium ions and from the decreasing spatial gradient of c. Within the time range $400 < t/\Delta t < 500$ the concentration s is unchanged. This reflects the irreversible character of the matrix dissolution as accounted for in the proposed model by the chemical internal parameter κ_c.

The $\log -s'/\log s'_{\max}$-plots in Fig. 5 illustrate the mass production s' due to matrix dissolution. For higher concentrations ($c \approx c_p$) the dissolution process is dominated by the portlandite dissociation at a high rate. The dissolution front propagates relatively fast through the specimen. In the initial phase of the dissolution process, no ettringite or CSH-phases are dissolved. As at the end of the chemical loading process the calcium concentration decreases to $c \approx c_{\text{csh}}$, a second maximum of s', corresponding to the dissolution of CSH-phases develops. Consequently, the first 250 time steps are controlled by the portlandite dissolution front and by the CSH dissolution at the end of the chemical loading. After the portlandite dissolution front has arrived at the end of the bar, all portlandite of the cement sample is dissolved. However, there remain chemically solvable cement phases in the material. The use of a logarithmic measure allows the visualization of the mass production s' also on smaller scales. The profiles of the negative dissociation rate $-s'$, illustrated in Fig. 6 for selected time steps, shows three maxima on different scales. The maximum propagating through the bar corresponds to the dissolution of portlandite, the second and third maxima are associated with the dissolution of ettringite and CSH-phases. Except for the profile for $t/\Delta t = 100$, where a high rate $\dot{c}$ at an already low level of calcium concentration c in the pore fluid is prescribed at the Dirichlet boundary, the portlandite mass production is more than one dimension larger compared to the CSH and ettringite dissolution. While the CSH dissolution profile is characterized by a small dissolution zone and a pronounced peak, the ettringite dissolution is characterized by a relatively broad dissolution zone and a small mass production s'. Hence, it can be observed that although the portlandite dominates the dissolution process, CSH and ettringite dissolution characterized by small rates of ion mass production always exists. This leads to the slow propagation of the CSH dissolution front relative to the portlandite front as was discussed earlier in the context of the distribution of s/s_0. It should be noted that the dissolution rate of the CSH and ettringite increases as soon as the portlandite has reached the end of the bar. This remarkable phenomenon results from the increase of $\dot{c}$ and, consequently, of the mass production of the remaining CSH- and ettringite phases after all portlandite is dissolved (see upper left graph of Fig. 5).

Next, the influence of the modeling of ion transport is investigated. In addition to the higher order transport model proposed in the first part of the paper, a standard transport model, characterized by a constant diffusivity of the pore fluid ($D_0 = D_{00}$, $D_{0c} = 0$) according to Fick (1855) is employed in the one-dimensional analyses of calcium leaching. The respective graph of the calcium concentration of the skeleton s is shown in Fig. 5. As expected, the portlandite as well as the CSH dissolution front are propagating faster compared to the results from the higher order transport model. Consequently, a faster progress of the material degradation and hence, a shorter life-time of the investigated structure is predicted if the standard transport model is applied. From Fig. 5 follows that the pronounced deceleration of the propagation of the

portlandite front with time is not predicted by Fick's transport model, since for this model the conductivity D_0 is not reduced by a decreasing calcium concentration. Therefore, a larger curvature of the portlandite dissolution front in the $s(X_2,t)$-diagram is obtained, if Kohlrausch's law is used to calculate the concentration dependent conductivity D_0.

3.1.3. Dimensional analysis of Ca^{2+} source terms

Fig. 7 contains the distributions of the source terms $s' = \dot{s}\Delta t$ and $c'_\phi = c'_{\phi 1} + c'_{\phi 2} = \dot{c}_{\phi 1}\Delta t + \dot{c}_{\phi 2}\Delta t = \dot{c}_\phi \Delta t$ (see part I of this paper Kuhl et al., in press) for $t/\Delta t = 100$ and $t/\Delta t = 200$. $\dot{c}_{\phi 1} = \dot{\phi}_c c$ and $\dot{c}_{\phi 1} = [\phi_0 + \phi_c]\dot{c}$ are associated with the change of the chemically induced porosity and the calcium concentration in the pore fluid, respectively. The left-hand side of Fig. 7 contains the individual source terms c'_ϕ, $c'_{\phi 1}$ and $c'_{\phi 2}$. On the right-hand side the level of the source term c'_ϕ can be compared with the level of the calcium mass production s' by dissociation. The relations between the source terms $c'_{\phi 1}$ and $c'_{\phi 2}$ obtained from investigations on the material point level in the first part of the paper (Kuhl et al., in press, Section 3.7) are verified by means of the plots given on the left-hand side of Fig. 7 in the cases of portlandite ($c'_{\phi 1}/c'_{\phi 2} \approx -14$, related data is marked in Fig. 7 by a circle) and ettringite ($c'_{\phi 2}/c'_{\phi 1} \approx -3$) dissolution for two selected time steps ($t/\Delta t = 100$ and $t/\Delta t = 200$). These values, and, in particular, the ratio for the CSH dissolution ($c'_{\phi 2}/c'_{\phi 1} \approx -0.85$) differ considerably from the values determined from dimensional analysis on the material point level (portlandite $c'_{\phi 1}/c'_{\phi 2} \approx -14$, ettringite $c'_{\phi 2}/c'_{\phi 1} \approx -6.5$ and CSH $c'_{\phi 2}/c'_{\phi 1} \approx -2.5$). These differences are resulting from the fact that now an initial-boundary value problem is solved, in which the spatial gradient ∇c has a strong influence on the level and propagation of the dissolution process. From the right-hand side of Fig. 7 follows, that, independent of the position and time, the dissolution rate $\dot{s}$ is at least 10^3 times larger than the source terms $\dot{c}_{\phi 1}$ and $\dot{c}_{\phi 2}$. The ratios $\dot{c}_{\phi 1}/\dot{s}$ and $\dot{c}_{\phi 2}/\dot{s}$ are obtained for the dissolution of portlandite as $-\dot{c}_{\phi 1}/\dot{s} \approx 14\dot{c}_{\phi 2}/\dot{s} \approx 6.5 \times 10^{-4}$, for the ettringite dissolution as $\dot{c}_{\phi 2}/\dot{s} \approx -3\dot{c}_{\phi 1}/\dot{s} \approx 1.25 \times 10^{-3}$, and for the CSH dissolution as $-\dot{c}_{\phi 1}/\dot{s} \approx 1.2\dot{c}_{\phi 2}/\dot{s} \approx 5 \times 10^{-5}$. The relation between the source terms $\dot{s}$ and $\dot{c}_\phi$ is of importance for the efficiency of finite element analyses of calcium leaching, since many terms of the effective internal flux r^i_c (Eq. (A.15)) and the tangent k^{ij}_{cc} (Eq. (A.17)) have to be calculated only for temporal and spatial discretization of the source term $\dot{c}_\phi$.

In conclusion, from the finite element analyses of a cement bar subjected to chemical dissolution according to the loading scenario 'standard analyses' (see Fig. 3) it follows that the source term $\dot{s}$ dominates the time scale of the dissolution–diffusion process for propagating chemical damage (chemical loading). Consequently, the source term $\dot{c}_\phi$ can be neglected without any noticeable influence on the precision of the simulation. However, if chemical unloading or non-proportional chemical loading occurs, the source term $\dot{c}_\phi$ seems to be essential to preserve the time dependent character of the local calcium mass balance.

To further validate this conclusion, an additional loading scenario, characterized by a shorter dissolution time (see the loading curve 'short-term dissolution' in Fig. 3) is investigated. The resulting profiles of the concentrations c/c_0 and s/s_0 and the dissolution rate $\dot{s}$ are plotted in Fig. 8. Profiles related to times ($t/\Delta t = 100, 200$) and to chemical unloading ($t/\Delta t \in [200, 300]$) are marked by gray and dashed lines, respectively. It is obvious that matrix dissolution at the end of the bar ($X_2 \in [60\text{ mm}, 80\text{ mm}]$) is still active in the chemical unloading range. Consequently, the concentrations c and s are further decreased within this region, the portlandite dissolution front still propagates and the dissolution rate is only marginally smaller compared with chemical loading. As a consequence of the propagating dissolution front during chemical unloading the characteristics of the dissolution–diffusion problem changes compared to the results for the loading scenario 'standard analyses' as given in Fig. 6. In contrast to Fig. 6 where chemical unloading is characterized by nearly horizontal c-profiles, representing a small time scale or a fast system change, the c-profiles in Fig. 8 illustrate a large time scale or a slow change of the non-linear system. Hence, it is concluded, that the transient behavior of the dissolution–diffusion system is governed by the source term $\dot{s}$ if in any subdomain of Ω matrix dissolution is active, i.e. $\dot{s} < 0$. With respect to the finite element implementation of the model, the computation of $\dot{c}_\phi$ and the related terms of the generalized vector of internal forces

and tangent stiffness matrix, respectively, may be disregarded without any loss of accuracy, if at any position $\boldsymbol{X} \in \Omega$ the dissolution rate is not zero ($\dot{s} < 0$ or, equivalently, $\dot{\kappa}_c < 0$). The efficiency of finite element analyses of dissolution–diffusion problems may be significantly improved, if these terms are only considered for $\dot{s} = 0 \ \forall \boldsymbol{X} \in \Omega$.

3.1.4. Propagation of dissolution fronts

As has been shown in the previous subsections, the dissolution fronts of calcium hydroxide and CSH-phases propagate through the cement specimen with different velocities. Since the velocity of dissolution fronts is a measure for the long-term degradation of cement materials, one-dimensional finite element analyses of a cement sample with the length $10L = 800$ mm based on the loading scenario 'long-term dissolution' (see Fig. 3) are performed (NE = 200 and $p = 5$). The resulting profiles of the Ca^{2+} mass production s' are given on the left-hand side of Fig. 9. In these profiles two pronounced maxima and a third, less pronounced maximum can be observed. The largest maximum of the curves represents the position of the portlandite dissolution front. The second largest maximum correlates with the position of the CSH dissolution front and the smallest maximum gives the position of maximum ettringite dissolution. The width of the dissolution zones grows with time while the velocity of the propagation decreases. On the right-hand side of Fig. 9 the positions of the dissolution fronts of portlandite and CSH-phases are plotted as functions of the square root of time. After the prescribed calcium concentration at the boundary has reached a minimum level at $t/\Delta t = 100$, i.e. at the end of chemical loading, the fronts associated with portlandite and CSH dissolution follow approximately straight lines. The positions of both dissolution fronts are proportional to $\sqrt{t}$. This observation is also described in many publications on calcium leaching (see e.g. Le Bellégo et al., 2000; Carde et al., 1996, 1997; Carde and François, 1997; Gérard et al., 1998; Mainguy et al., 2000, 2001; Mainguy and Ulm, 2000; Torrenti et al., 1998). Compared to the dissolution front of CSH-phases ($X_2 = 0.049 \frac{\text{mm}}{\sqrt{\text{d}}} \sqrt{t} = 0.94 \frac{\text{mm}}{\sqrt{\text{a}}} \sqrt{t}$) the portlandite dissolution front ($X_2 = 0.35 \frac{\text{mm}}{\sqrt{\text{d}}} \sqrt{t} = 6.69 \frac{\text{mm}}{\sqrt{\text{a}}} \sqrt{t}$) propagates significantly faster. The constant $6.69 \frac{\text{mm}}{\sqrt{\text{a}}}$ corresponds well with the respective constant reported by Le Bellégo et al. (2000) for a cement paste with a high water to cement ratio. If the movement of the ettringite dissolution zone is estimated based on the maximum ettringite dissolution, its velocity is situated between both pronounced dissolution fronts. For more detailed comparisons of standard transport models using Fick's law (1855) and higher order transport models considering ion–ion interactions and the associated propagation of dissolution fronts see (Kuhl, submitted for publication; Kuhl and Meschke, 2002).

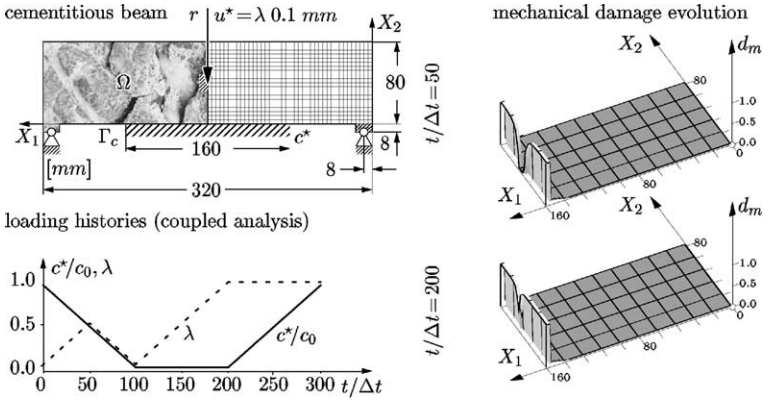

Fig. 10. Chemo-mechanical analysis of a cementitious beam: geometry, boundary conditions, loading histories and discretization. Evolution of the mechanical damage parameter d_m.

3.2. Coupled calcium leaching and damage of a cementitious beam

In order to illustrate the interaction of chemically and mechanically induced damage the behavior of a cementitious beam under plane strain conditions, subjected to cyclic mechanical loading and chemical attack, is simulated by using the proposed coupled material model and discretization technique. The left-hand side of Fig. 10 contains the geometry, the mechanical load, the mechanical support conditions, the chemical Dirichlet boundary Γ_c, the discretization by finite elements with $p = 1$ and the time history of the applied mechanical and chemical loads. The material data (Table 1) are identical to the previous section. The initial conditions are given by $\boldsymbol{u}_0 = \boldsymbol{0}$ (undeformed configuration) and $c(t_0) = c_0$ (chemical equilibrium state of the virgin cement paste) within the domain Ω. The Neumann boundary conditions are prescribed as $q^\star = 0$ for $\boldsymbol{X} \in \Gamma_q$ (insulated surfaces) and $\boldsymbol{t}^\star = \boldsymbol{0}$ for $\boldsymbol{X} \in \Gamma_\sigma$. A displacement driven load is applied in the hatched region (equivalent to four finite elements) at the center of the beam. In this region, a larger initial damage threshold $\kappa_m^{0\prime} = 10^4 \kappa_m^0$ and a smaller Young's modulus $E_s' = E_s/2$ was used to avoid local damage resulting from a concentrated load. The application of the mechanical load in two loading steps and one unloading step is controlled by the load parameter λ. Chemical loading is applied by prescribing a time variant calcium concentration $c^\star$ at the bottom of the beam. The calcium concentration $c^\star$ is decreased from an initial equilibrium concentration of the sound material ($c^\star/c_0 = 1$) to $c^\star/c_0 = 0$, representing deionized water, and subsequently increased again to the initial equilibrium concentration $c^\star/c_0 = 1$. For the time integration the parameters $\alpha = 2\beta = \gamma = 0.5$ and the time step $\Delta t = 275$ d are used.

3.2.1. Discussion of coupled chemo-mechanical damage

The right-hand side of Fig. 10 contains distributions of the mechanical damage parameter d_m at two stages of loading. Since the ill-posed elasto-damage problem has not been regularized, damage is restricted to one column of elements. As expected from the simple scalar damage model used in this analysis, which gives the same response in tension and compression, damage propagates from the bottom and the top of the beam towards the center. As a result of chemical attack along at the bottom of the beam, however, the damage distribution is non-symmetric with respect to the line $X_2 = 40$ mm.

Fig. 11 illustrates, from the left to the right-hand side, the normalized calcium concentration of the pore fluid c/c_0, the concentration of the remaining calcium in the skeleton s/s_0 and the calcium dissolution rate $s' = \dot{s}\Delta t$ for selected time steps. A logarithmic measure normalized with respect to the maximum dissolution rate $s'_{\max} = -1327$ mol/m^3 is used to visualize the portlandite, ettringite and CSH dissolution rates (values $-s' < 1$ mol/m^3 are set to $-s' = 1$ mol/m^3). From the top to the bottom, the first four graphs ($t/\Delta t \in [0, 200]$) correspond to chemical loading and the last two graphs ($t/\Delta t \in [250, 300]$) correspond to unloading. During chemical loading the reduction of the prescribed concentration $c^\star$ at Γ_c and the reduction of c within Ω can be observed. As a consequence of the decreasing calcium concentration c, chemical equilibrium between the skeleton and the pore water is violated and portlandite of the skeleton is instantaneously dissociated. The portlandite dissolution front, characterized by a high gradient of the concentration s and by a peak of the matrix dissolution rate s' propagates through the beam. At $t/\Delta t = 100$ a second front associated with the dissolution of CSH can be observed in the $\log -s'/\log s'_{\max}$-plots. In the s/s_0-plots, these two pronounced dissolution fronts are represented by two distinct steps. Between the portlandite and CSH fronts ettringite is dissolved at a much lower rate. The distribution of the calcium concentration c of the pore fluid is approximately linear. The dissolution fronts propagate faster in the damage zone close to the axis of symmetry ($X_1 = 80$ mm) compared to other regions of the beam, because the apparent pore space and the macroscopic conductivity are increased by mechanically induced damage. Consequently, the propagation of the dissolution front is accelerated due to mechanical damage.

In the phase of chemical unloading the concentration c is increased in the vicinity of the lower face of the beam by the reflux of calcium ions. In the region of the portlandite dissolution front, however, the concentration c further decreases and the dissolution front continues to destroy the cement paste. At the end of

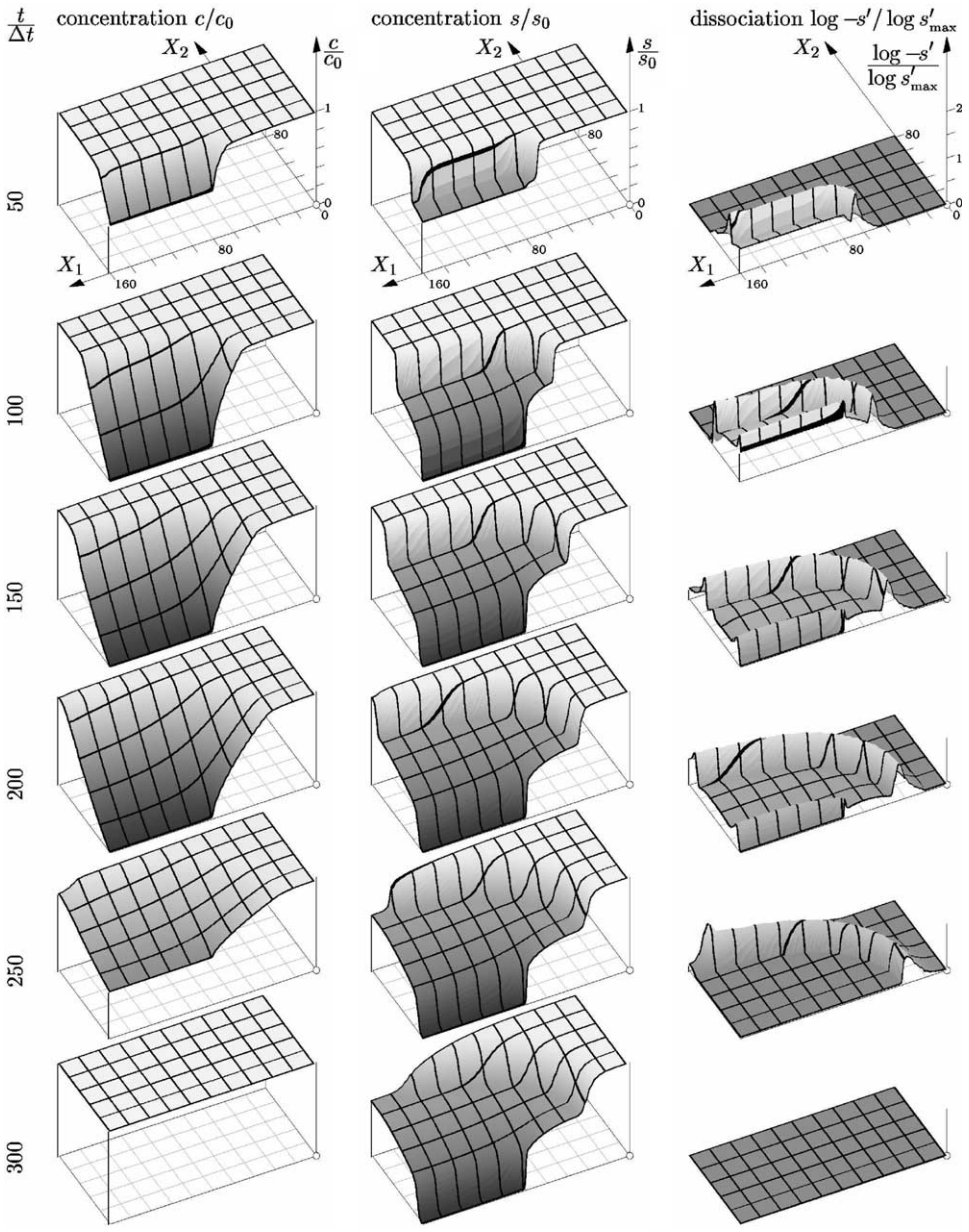

Fig. 11. Chemo-mechanical analysis of a cementitious beam: evolution of c/c_0, s/s_0 and $\log -s'/\log s'_{max}$ (X_1, X_2 [mm]).

the analysis the initial concentration of calcium ions in the pore space is recovered and the chemical degradation process is stopped ($s' = 0$) but the increase of the porosity, represented by the state of s, is permanent.

3.2.2. Interaction of chemically and mechanically induced material deterioration

To obtain a deeper insight into the interactions between mechanical and chemical material degradation, results from the coupled chemo-mechanical analysis are compared to uncoupled purely mechanical and

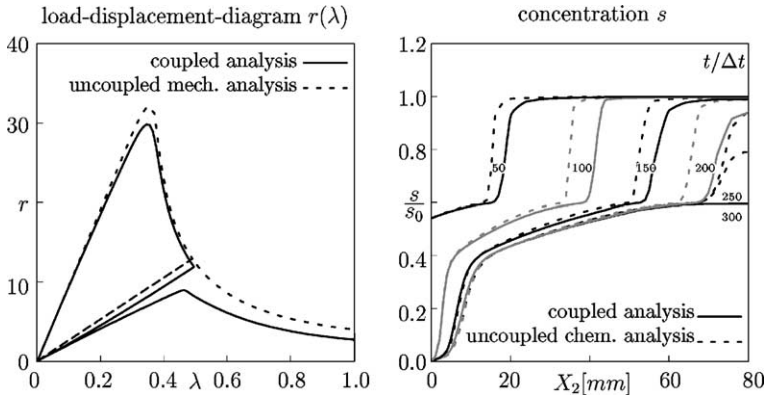

Fig. 12. Chemo-mechanical analysis of a cementitious beam: load–displacement diagrams $r(\lambda)$ [N] and calcium concentration profiles s/s_0 at position $X_1 = 160$ mm for coupled and uncoupled analyses.

chemical analyses of the cementitious beam. The left-hand side of Fig. 12 shows the load–displacement diagrams obtained from a coupled chemo-mechanical analysis and from a purely mechanical analysis.

As expected from the material point studies in the first part of the paper (Kuhl et al., in press), the stiffness and strength of the beam are reduced by calcium leaching. This observation corresponds with the three-point bending tests of cement beams subjected simultaneously to accelerated leaching by applying an ammonium nitrate solution at the bottom of the beam by Le Bellégo et al. (2000, 2001a,b). Furthermore, the degradation of structural stiffness and the decreasing limit load due to calcium leaching was observed by Le Bellégo et al. (2000, 2001a,b). In their experiments the lateral faces of cement beams are exposed to an ammonium nitrate solution. The duration of the exposure varies in the different tests. Subsequently displacement controlled bending tests are performed. Compared with a pure mechanical experiment, these tests show the reduction of structural stiffness and of the limit load due to chemical degradation. In Fig. 12 the un- and re-loading paths are different, because the porosity continues to decrease in the unloading/loading cycles due to chemical dissolution. Due to chemical softening the damage threshold κ_m is apparently reduced during the reloading of the beam. In Fig. 13 the influence of chemical softening on the structural level is investigated by comparing the distributions of the normal stress $\sigma_{11}(X_1)$ for the uncoupled (purely mechanical) and the coupled chemo-mechanical analyses at two selected positions X_1. In the uncoupled analysis, the stress distributions at $t/\Delta t = 50$ and $t/\Delta t = 150$ are identical and for $t/\Delta t > 200$ the stress state does not change. The largest stress is obtained at $t/\Delta t = 150$. In the coupled analysis the largest stress is obtained at $t/\Delta t = 50$. The stress distribution across the height of the beam is only slightly changed for $t/\Delta t = 200$. In contrast to the purely mechanical simulation the stress distributions at $t/\Delta t = 50$ and $t/\Delta t = 150$ are not identical. At $t/\Delta t = 150$ the peak stress is significantly reduced due to chemical softening. In addition to the stress level also the stress distribution is affected by chemical damage. The softening effect of propagating portlandite and CSH dissolution fronts is manifested in the graphs associated with $X_1 = 60$ mm and, less pronounced, in the graphs for $X_1 = 80$ mm by more or less strong steps in the stress profiles. These steps are associated with the loss of stiffness resulting from the dissolution of portlandite ($t/\Delta t = 50$) and CSH for $t/\Delta t \geqslant 150$ (compare the s/s_0-distribution in Fig. 11). The marginal variations of the stress distributions for $t/\Delta t \geqslant 200$ are related to the movement of the portlandite dissolution front. Chemical softening propagating from the bottom face upwards results in a changing position of the neutral axis of the beam towards positive X_2 coordinates. Consequently, the damage distribution is non-symmetric with respect to the symmetry axis $X_2 = 40$ mm. Furthermore, chemical softening accelerates the damage propagation of structures (compare Fig. 10). It is concluded that chemical damage may have a

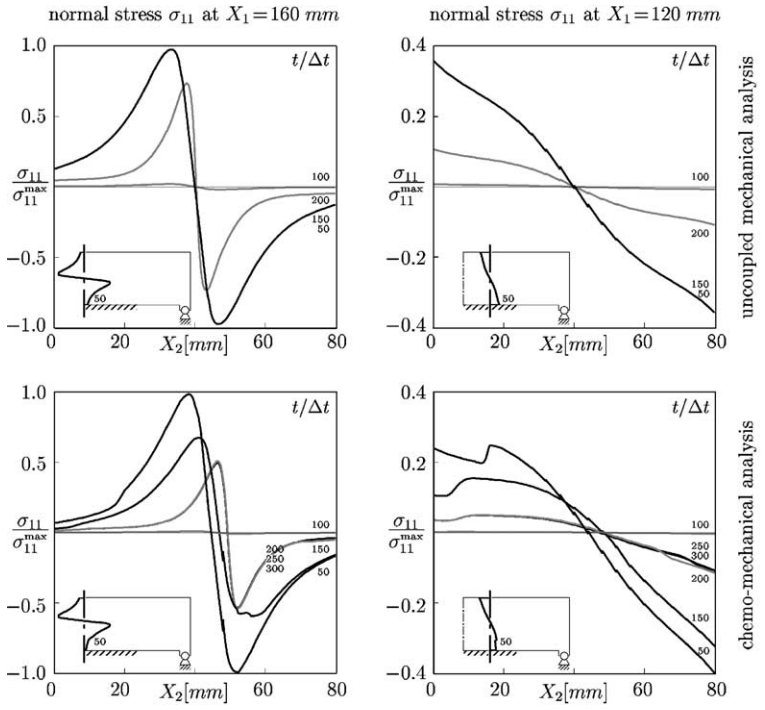

Fig. 13. Chemo-mechanical analysis of a cementitious beam: distribution of the normal stress component $\sigma_{11}/\sigma_{11}^{\max}$ ($\sigma_{11}^{\max} = 3.4214$ N/mm^2) at positions $X_1 = 160$ mm and $X_1 = 120$ mm.

considerable influence on the structural behavior since not only the critical load is reduced by chemically induced deterioration but also the stress distribution, and hence, the failure mode may be changed by chemical dissolution processes.

On the right-hand side of Fig. 12 the profiles of the calcium content in the skeleton along the axis of symmetry obtained for uncoupled (purely chemical) and coupled chemo-mechanical analyses are plotted at different time steps. It is obvious that the portlandite dissolution front propagates faster if mechanical damaged is considered in the analysis. As a consequence of the slower propagation of the portlandite dissolution front in the purely mechanical analysis, a larger concentration gradient ∇c is computed which results in a (marginally) faster propagation of the CSH dissolution front compared with the coupled chemo-mechanical analysis. Since the total porosity $\phi = \phi_0 + \phi_c + [1 - \phi_0 - \phi_c]d_m$ is increased by mechanical damage, the macroscopic diffusivity ϕD_0 is also increased. Consequently, the velocity of chemical degradation is increased by mechanical damage (compare material point studies in the first part of the paper Kuhl et al., in press). The acceleration of calcium leaching due to mechanical damage can also be observed during the durability tests of beams subjected simultaneously to chemical and mechanical loads performed by Le Bellégo et al. (2001a).

3.2.3. Ultimate load tests at different states of calcium leaching

In this section, the influence of calcium leaching to the residual ultimate load and stiffness of concrete structures is demonstrated. For this purpose, the cementitious beam illustrated in Fig. 10 is analyzed mechanically at different stages of chemical degradation. In the first part of the numerical experiment, a prescribed calcium concentration $c^\star/c_0 = \langle 1 - t/[100\Delta t]\rangle$ is applied at the chemical Dirichlet boundary $\boldsymbol{X} \in \Gamma_c$. After six stages of chemical exposure, characterized by the exposure time T_c with

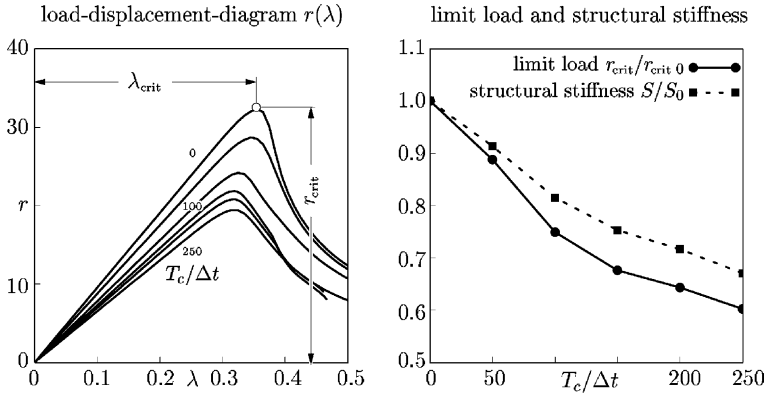

Fig. 14. Load–displacement diagrams $r(\lambda)$ [N] for different states of chemical degradation characterized by the chemical exposure time T_c. Reduction of the limit load r_{crit} and the structural stiffness $S = r_{crit}/u^{\star}_{crit}$ for $u^{\star}_{crit} = \lambda_{crit}0.1$ mm normalized with respect to $r_{crit\,0}$ and S_0 from a purely mechanical analysis ($T_c/\Delta t = 0$).

$T_c/\Delta t \in [0, 50, 100, 150, 200, 250]$, the chemical dissolution state is frozen. In the second part of the numerical experiment, purely mechanical, displacement controlled ultimate load tests using the leached cementitious beam samples are performed.

On the right-hand side of Fig. 12 the state of chemical degradation for $T_c/\Delta t \in [0, 50, 100, 150, 200]$ of the uncoupled chemical analysis is illustrated by means of the calcium concentration of the skeleton s/s_0. Since, in contrast to the present analysis, in Fig. 12 chemical unloading for $T_c/\Delta t > 200$ is considered, only the profiles for $T_c/\Delta t < 250$ can be considered. On the left-hand side of Fig. 14 the resulting load–displacement diagrams are shown. As expected, from the material studies in the first part of the paper (Kuhl et al., in press) and from the structural analyses in the previous sections, the following observations are made: The limit load r_{crit} of the cementitious beam and the structural stiffness $S = r_{crit}/[\lambda_{crit}0.1\text{ mm}]$ are significantly reduced by calcium leaching. Furthermore, the slope of the load–displacement diagrams in the post-critical regime indicate that the brittleness of the structure is slightly decreased. Analogous statements concerning the structural effects of calcium leaching have been given by Le Bellégo et al. (2000, 2001a,b, 2003) based on experimental investigations on concrete beams subjected to accelerated leaching. It is worth to mention that the load–displacement diagrams $r(\lambda)$ for the leaching times $T_c/\Delta t = 150$ and $T_c/\Delta t = 200$ show a different post-critical structural behavior compared with the remaining curves. The kink in the softening branch of the curves $T_c/\Delta t = 150$ and $T_c/\Delta t = 200$ corresponds to a stage of chemical damage, in which the leaching front has reached the loading zone (i.e. the hatched region in Fig. 10). Load re-distribution of stresses in this area leads to a faster propagation of mechanically induced damage. On the right-hand side of Fig. 14 the limit load and the structural stiffness are plotted as function of the leaching time T_c. This diagram shows the considerable reduction of the limit load and the structural stiffness with increasing chemical degradation. At $T_c/\Delta t = 250$ the limit load and the structural stiffness are reduced by 40% and 30%, respectively.

4. Conclusions

This paper describes the finite element strategy used for coupled numerical analysis of long-term structural deterioration based upon the chemo-mechanical model for cementitious materials presented in the companion paper (Kuhl et al., in press) together with representative results from finite element durability analyses. The chemo-mechanical model accounts for the damage induced by external loading

and chemical dissolution of calcium and the interactions of both mechanisms. It is based upon the theory of mixtures. The associated coupled field problem is described by the mass balance of dissolved calcium ions, the balance of linear momentum and related constitutive laws. Ingredients of the numerical solution procedure are a second order accurate time marching scheme, the spatial discretization by means of hierarchically generated higher order finite elements and the iterative Newton–Raphson solution technique. Representative numerical experiments demonstrate the applicability of the chemo-mechanical model and the numerical methods for the simulation of long-term degradation of structures made of cementitious materials due to calcium leaching and mechanical induced damage. From a detailed one-dimensional study of calcium leaching of a cementitious bar the following conclusions are drawn:

(1) The propagation of pronounced dissolution fronts associated with the dissolution of portlandite and CSH-phases is proportional to $\sqrt{t}$. The dissolution of ettringite has a relatively minor influence.
(2) Calcium leaching is irreversible.
(3) Dissolution of the cementitious skeleton accelerates the calcium ion transport and, consequently, the propagation of dissolution fronts and the chemical degradation of concrete structures.
(4) The time scale of dissociation–diffusion processes may significantly change during the numerical analysis.
(5) The source term $[[\phi_0 + \phi_c]c]^{\cdot}$, which accounts for the change of the porosity and the calcium concentration in the pore fluid, can be neglected compared to the matrix dissolution rate $\dot{s}$. It may not be neglected in the case of chemical unloading ($\dot{s} = 0$).

An insight into interacting mechanisms between chemical dissolution processes and mechanically induced damage on a structural level is provided by numerical analyses of a concrete beam subjected simultaneously to chemical attack and mechanical loading. From the comparison of coupled and uncoupled analyses as well as the sequentially performed chemical and mechanical analyses the following observations were made:

(1) Calcium leaching reduces the stiffness and the limit load of structures.
(2) The brittleness of the structure is slightly decreased by calcium leaching.
(3) Calcium leaching changes the structural behavior.
(4) Mechanically induced damage not only results in the degradation of strength and stiffness of cementitious materials but also amplifies the chemical degradation process.

Acknowledgements

Financial support was provided by the German National Science Foundation (DFG) in the framework of project A9 of the collaborative research center (SFB) 398. This support is gratefully acknowledged.

Appendix A. Finite element quantities

In this appendix the hierarchically generated shape functions, their derivatives with respect to the natural coordinates, the Jacobi transformation, the generalized vector of residual forces and the generalized tangent stiffness matrix are summarized for fully coupled chemo-mechanical two-dimensional elements are formulated within the framework of the *p*-finite element method.

A.1. Hierarchical generation of shape functions

For a systematic generation of higher order shape functions the hierarchical concept described by Szabó and Babuška (1992) is used. The shape functions of the polynomial degree p are generated by four-nodal shape functions related to the nodal coordinates ξ_1^i and ξ_2^i,

$$N^i(\boldsymbol{\xi}) = \tfrac{1}{4}[1+\xi_1^i\xi_1][1+\xi_2^i\xi_2] \quad i=1,2,3,4 \tag{A.1}$$

by $4[p-1]$ side modes

$$\begin{aligned} N^{4i-3}(\boldsymbol{\xi}) &= \tfrac{1}{2}[1-\xi_2]\Phi^i(\xi_1) \\ N^{4i-2}(\boldsymbol{\xi}) &= \tfrac{1}{2}[1+\xi_1]\Phi^i(\xi_2) \\ N^{4i-1}(\boldsymbol{\xi}) &= \tfrac{1}{2}[1+\xi_2]\Phi^i(\xi_1) \\ N^{4i}(\boldsymbol{\xi}) &= \tfrac{1}{2}[1-\xi_1]\Phi^i(\xi_2) \end{aligned} \qquad i=2,3,4,\ldots,p \tag{A.2}$$

and, finally for $p>3$, by $[p-2][p-3]/2$ internal modes, compare Table 3.

$$N^{4p+k}(\boldsymbol{\xi}) = \Phi^i(\xi_1)\Phi^j(\xi_2) \quad i,j=2,3,4,\ldots,p-2,\ i+j\leqslant p \tag{A.3}$$

Table 3
Hierarchically generated shape functions based on Legendre polynomials

p	nodal and side modes	internal modes
1	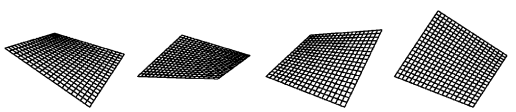	
2	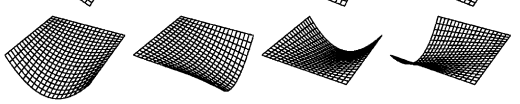	
3	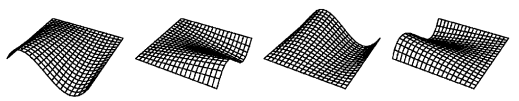	
4	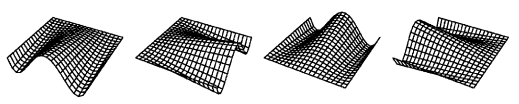	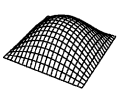
5	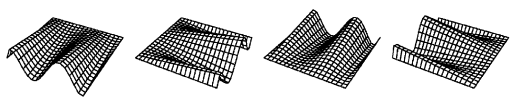	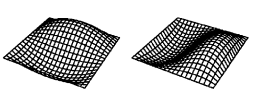
6	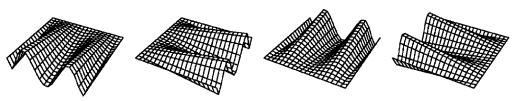	
7	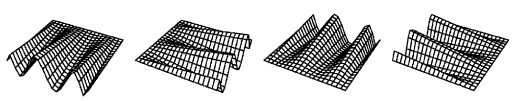	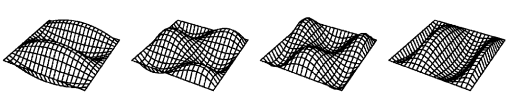

Internal modes are numbered consecutively by $k \in [1,[p-2][p-3]/2]$. The functions $\Phi^i(\xi_\alpha)$, $\alpha = 1,2$, are defined in terms of Legendre polynomials $P^i(\xi_\alpha)$ with the polynomial degree i,

$$\Phi^i(\xi_\alpha) = \frac{1}{\sqrt{2[2i-1]}}[P^i(\xi_\alpha) - P^{i-2}(\xi_\alpha)] \tag{A.4}$$

which can be generated by Bonnet's recursion formula:

$$P^i(\xi_\alpha) = \frac{2i-1}{i}\xi_\alpha P^{i-1}(\xi_\alpha) - \frac{i-1}{i}P^{i-2}(\xi_\alpha) \quad i = 2,3,\ldots,p \tag{A.5}$$

The roots of Eq. (A.5) are defined by constant and linear functions of the natural coordinate ξ_α:

$$P^0(\xi_\alpha) = 1, \qquad P^1(\xi_\alpha) = \xi_\alpha \tag{A.6}$$

The derivatives of the shape functions with respect to the natural coordinates $\boldsymbol{\xi} = [\xi_1 \;\; \xi_2]^{\mathrm{T}}$ are also generated systematically. The derivatives $\partial N^i/\partial\xi_\alpha = N^i_{,\alpha}$ of the nodal shape functions, the side—and the internal modes

$$\begin{aligned}
&N^i_{,1}(\boldsymbol{\xi}) = \xi^i_1[1+\xi^i_2\xi_2]/4 && N^i_{,2}(\boldsymbol{\xi}) = \xi^i_2[1+\xi^i_1\xi_1]/4\\
&N^{4i-3}_{,1}(\boldsymbol{\xi}) = [1-\xi_2]\Phi^i_{,1}(\xi_1)/2 && N^{4i-3}_{,2}(\boldsymbol{\xi}) = [-1]\Phi^i(\xi_1)/2\\
&N^{4i-2}_{,1}(\boldsymbol{\xi}) = \Phi^i(\xi_2)/2 && N^{4i-2}_{,2}(\boldsymbol{\xi}) = [1+\xi_1]\Phi^i_{,2}(\xi_2)/2\\
&N^{4i-1}_{,1}(\boldsymbol{\xi}) = [1+\xi_2]\Phi^i_{,1}(\xi_1)/2 && N^{4i-1}_{,2}(\boldsymbol{\xi}) = \Phi^i(\xi_1)/2\\
&N^{4i}_{,1}(\boldsymbol{\xi}) = [-1]\Phi^i(\xi_2)/2 && N^{4i}_{,2}(\boldsymbol{\xi}) = [1-\xi_1]\Phi^i_{,2}(\xi_2)/2\\
&N^{4p+k}_{,1}(\boldsymbol{\xi}) = \Phi^i_{,1}(\xi_1)\Phi^j(\xi_2) && N^{4p+k}_{,2}(\boldsymbol{\xi}) = \Phi^i(\xi_1)\Phi^j_{,2}(\xi_2)
\end{aligned} \tag{A.7}$$

are calculated based on the derivatives $\Phi^i_{,\alpha}$, $\alpha = 1,2$, given in terms of the derivatives of the Legendre polynomials:

$$\begin{aligned}
&\Phi^i_{,\alpha}(\xi_\alpha) = [P^i_{,\alpha}(\xi_\alpha) - P^{i-2}_{,\alpha}(\xi_\alpha)]/\sqrt{2[2i-1]}, \quad P^0_{,\alpha}(\xi_\alpha) = 0\\
&P^i_{,\alpha}(\xi_\alpha) = [2i-1]P^{i-1}(\xi_\alpha) + P^{i-2}_{,\alpha}(\xi_\alpha), \quad P^1_{,\alpha}(\xi_\alpha) = 1
\end{aligned} \tag{A.8}$$

As the shape functions are described in natural coordinates $\boldsymbol{\xi} = [\xi_1 \;\; \xi_2]^{\mathrm{T}}$ the Jacobi transformations have to be applied:

$$\nabla N^i = \frac{\partial N^i}{\partial \boldsymbol{\xi}} \cdot \frac{\partial \boldsymbol{\xi}}{\partial \boldsymbol{X}} = \boldsymbol{J}^{-\mathrm{T}} \cdot \nabla_\xi N^i, \qquad \mathrm{d}V = \mathrm{d}A h = |\boldsymbol{J}|\,\mathrm{d}\xi_1\,\mathrm{d}\xi_2 h \tag{A.9}$$

Here, $\mathrm{d}\xi_3 = h$ is the element thickness of plane elements, $\boldsymbol{J}$ is the Jacobian and $\nabla_\xi N^i$ is the gradient of the shape function N^i with respect to the natural coordinates $\boldsymbol{\xi}$:

$$\boldsymbol{J} = \frac{\partial \boldsymbol{X}}{\partial \boldsymbol{\xi}} \approx \sum_{i=1}^{m} \boldsymbol{X}^i \otimes \nabla_\xi N^i, \qquad \nabla_\xi N^i = \frac{\partial N^i}{\partial \boldsymbol{\xi}} \tag{A.10}$$

The integration of element vectors and matrices is performed over the two-dimensional domain by the Gauss quadrature,

$$\int_{-1}^{1}\int_{-1}^{1}(\cdot)(\xi_1,\xi_2)\,\mathrm{d}\xi_1\,\mathrm{d}\xi_2 \approx \sum_{l=1}^{\mathrm{gp}}\sum_{q=1}^{\mathrm{gp}}\alpha^l_1\alpha^q_2(\cdot)(\xi^l_1,\xi^q_2) \tag{A.11}$$

where the number of Gauss points 'gp' is related to the highest polynomial degree, such that a full integration is guaranteed. For the natural coordinates of the Gauss points ξ_1^l and ξ_2^q and the weights α_1^l and α_2^q (see Szabó and Babuška, 1992).

A.2. Generalized vector of internal forces

Considering the hierarchical finite element approximation of the geometry (10), the Jacobian can be calculated:

$$\boldsymbol{J} \approx \sum_{i=1}^{m} \boldsymbol{X}^i \otimes \nabla_{\xi} N^i \tag{A.12}$$

$\boldsymbol{\gamma}$, $\delta\boldsymbol{\gamma}$, $\Delta\boldsymbol{\gamma}$, $\nabla\boldsymbol{u}$ and $\boldsymbol{\varepsilon}$ are discretized by computing the gradient of the shape functions ∇N^i (A.9):

$$\boldsymbol{\gamma} \approx -\sum_{i=1}^{m} c^i \nabla N^i, \qquad \nabla\boldsymbol{u} \approx \sum_{i=1}^{m} \boldsymbol{u}^i \otimes \nabla N^i, \qquad \boldsymbol{\varepsilon} = \nabla^{\mathrm{sym}}\boldsymbol{u} \tag{A.13}$$

Using the symmetry of the stress tensor $\boldsymbol{\sigma}$ the approximation of the variation of the specific strain energy is given in the following format:

$$\delta\boldsymbol{\varepsilon} : \boldsymbol{\sigma} \approx \sum_{i=1}^{m} \delta\boldsymbol{u}^i \cdot \nabla N^i \cdot \boldsymbol{\sigma} \tag{A.14}$$

With these approximations the tensor valued components of the generalized vector of residual forces $\boldsymbol{r} - \boldsymbol{r}_e$, given in terms of the generalized internal $\boldsymbol{r}$ and external forces $\boldsymbol{r}_e$, are computed, compare Eq. (11):

$$\begin{aligned}
r^i_{cn+1-\alpha} &= -\int_{\Omega} \nabla N^i \cdot \boldsymbol{q}_{n+1-\alpha}\,\mathrm{d}V + \int_{\Omega} N^i[[\phi_0 + \phi_c]\dot{c} + \dot{\boldsymbol{\phi}}_c c + \dot{s}]_{n+1-\alpha}\,\mathrm{d}V \\
r^i_{ce\,n+1-\alpha} &= \int_{\Gamma_q} N^i q^{\bigstar}_{n+1-\alpha}\,\mathrm{d}A \\
\boldsymbol{r}^i_{m\,n+1-\alpha} &= \int_{\Omega} \nabla N^i \cdot \boldsymbol{\sigma}_{n+1-\alpha}\,\mathrm{d}V \\
\boldsymbol{r}^i_{me\,n+1-\alpha} &= \int_{\Gamma_\sigma} N^i \boldsymbol{t}^{\bigstar}_{n+1-\alpha}\,\mathrm{d}A
\end{aligned} \tag{A.15}$$

A.3. Generalized tangent stiffness matrix

Approximations (10) and the symmetry of the stress and constitutive tensors allow the discretization of the individual terms included in the linearized internal virtual work (7):

$$\begin{aligned}
\delta\boldsymbol{\varepsilon} : \frac{\partial\boldsymbol{\sigma}}{\partial\boldsymbol{\varepsilon}} : \Delta\boldsymbol{\varepsilon} &\approx \sum_{i=1}^{m}\sum_{j=1}^{m} \delta\boldsymbol{u}^i \cdot \nabla N^i \cdot \frac{\partial\boldsymbol{\sigma}}{\partial\boldsymbol{\varepsilon}} \cdot \nabla N^i \cdot \Delta\boldsymbol{u}^j \\
\delta\boldsymbol{\varepsilon} : \frac{\partial\boldsymbol{\sigma}}{\partial c}\Delta c &\approx \sum_{i=1}^{m}\sum_{j=1}^{m} \delta\boldsymbol{u}^i \cdot \nabla N^i \cdot \frac{\partial\boldsymbol{\sigma}}{\partial c} N^i \Delta c^j
\end{aligned} \tag{A.16}$$

Finally, the tensor valued components of the generalized tangent stiffness matrix $\mathbf{K}^t$ (compare Eq. (11)) are calculated as

$$
\begin{aligned}
\boldsymbol{k}^{ij}_{cm} &= -\int_\Omega \nabla N^i \cdot \left[\frac{\partial \boldsymbol{q}}{\partial \boldsymbol{\varepsilon}}\right]_{n+1-\alpha} \cdot \nabla N^j \frac{\partial \boldsymbol{u}_{n+1-\alpha}}{\partial \boldsymbol{u}_{n+1}} \mathrm{d}V \\
k^{ij}_{cc} &= -\int_\Omega \nabla N^i \cdot \left[\frac{\partial \boldsymbol{q}}{\partial c}\right]^c_{n+1-\alpha} N^j \frac{\partial c_{n+1-\alpha}}{\partial c_{n+1}} \mathrm{d}V \\
&\quad + \int_\Omega \nabla N^i \cdot [\phi \boldsymbol{D}_0]_{n+1-\alpha} \cdot \nabla N^j \frac{\partial c_{n+1-\alpha}}{\partial c_{n+1}} \mathrm{d}V \\
&\quad + \int_\Omega N^i \left[\frac{\partial s}{\partial c}\right]_{n+1-\alpha} 2 \frac{\partial \phi_c}{\partial s} \dot{c}_{n+1-\alpha} N^j \frac{\partial c_{n+1-\alpha}}{\partial c_{n+1}} \mathrm{d}V \\
&\quad + \int_\Omega N^i \left[\frac{\partial^2 s}{\partial \kappa_c^2}\right]_{n+1-\alpha} \phi_s \frac{\partial \kappa_c}{\partial c} \dot{c}_{n+1-\alpha} N^j \frac{\partial c_{n+1-\alpha}}{\partial c_{n+1}} \mathrm{d}V \\
&\quad + \int_\Omega N^i \left[\frac{\partial s}{\partial c}\right]_{n+1-\alpha} \phi_s N^j \frac{\partial \dot{c}_{n+1-\alpha}}{\partial \dot{c}_{n+1}} \frac{\partial \dot{c}_{n+1}}{\partial c_{n+1}} \mathrm{d}V \\
&\quad + \int_\Omega N^i [\phi_0 + \phi_{cn+1-\alpha}] N^j \frac{\partial \dot{c}_{n+1-\alpha}}{\partial \dot{c}_{n+1}} \frac{\partial \dot{c}_{n+1}}{\partial c_{n+1}} \mathrm{d}V \\
\boldsymbol{k}^{ij}_{mm} &= \int_\Omega \nabla N^i \cdot \left[\frac{\partial \boldsymbol{\sigma}}{\partial \boldsymbol{\varepsilon}}\right]_{n+1-\alpha} \cdot \nabla N^j \frac{\partial \boldsymbol{u}_{n+1-\alpha}}{\partial \boldsymbol{u}_{n+1}} \mathrm{d}V \\
\boldsymbol{k}^{ij}_{mc} &= \int_\Omega \nabla N^i \cdot \left[\frac{\partial \boldsymbol{\sigma}}{\partial c}\right]_{n+1-\alpha} N^j \frac{\partial c_{n+1-\alpha}}{\partial c_{n+1}} \mathrm{d}V
\end{aligned}
\tag{A.17}
$$

where the abbreviation

$$
\left[\frac{\partial \boldsymbol{q}}{\partial c}\right]^c_{n+1-\alpha} = \left[[1-d_m] \frac{\partial \phi_c}{\partial s} \frac{\partial s}{\partial \kappa_c} \frac{\partial \kappa_c}{\partial c} \boldsymbol{D}_0 \cdot \boldsymbol{\gamma} + \phi \frac{\partial \boldsymbol{D}_0}{\partial c} \cdot \boldsymbol{\gamma}\right] \tag{A.18}
$$

is used. ϕ_s is defined by Eq. (8).

References

Adenot, F., Buil, M., 1992. Modelling of the corrosion of the cement paste by deionized water. Cement and Concrete Research 22, 489–496.

Bangert, F., 1999. Entwicklung eines hierarchisch generierten finiten Mehrfeldelementes am Beispiel der thermo-mechanischen Kopplung. Master's thesis, Institute for Structural Mechanics, Ruhr University Bochum.

Becker, C., 2001. Untersuchung räumlicher Diskretisierungsmethoden zur Simulation nichtlinearer Reaktions–Diffusions Probleme. Master's thesis, Institute for Structural Mechanics, Ruhr University Bochum.

Belytschko, T., Liu, W., Moran, B., 2000. Nonlinear Finite Elements for Continua and Structures. John Wiley, Chicester.

Berner, U., 1988. Modelling the incongruent dissolution of hydrated cement minerals. Radiochimica Acta 44–45, 387–393.

Bowen, R., 1976. Theory of mixtures. In: Eringen, A. (Ed.), Continuum Physics. Academic Press, New York, pp. 1–127.

Carde, C., François, R., 1997. Effect on the leaching of calcium hydroxide from cement paste on mechanical properties. Cement and Concrete Research 27, 539–550.

Carde, C., François, R., Torrenti, J.-M., 1996. Leaching of both calcium hydroxide and C–S–H from cement paste: modelling the mechanical behavior. Cement and Concrete Research 22, 1257–1268.

Carde, C., Escadeillas, G., François, R., 1997. Use of ammonium nitrate solution to simulate and accelerate the leaching of cemente pastes due to deionized water. Magazine of Concrete Research 49, 295–301.

Chung, J., Hulbert, G., 1993. A time integration algorithm for structural dynamics with improved numerical dissipation: the generalized-α method. Journal of Applied Mechanics 60, 371–375.

Crisfield, M., 1991. Non-Linear Finite Element Analysis of Solids and Structures. Volume 1: Essentials. John Wiley, Chicester.

Crisfield, M., 1997. Non-Linear Finite Element Analysis of Solids and Structures. Volume 2: Advanced Topics. John Wiley, Chicester.

Díez, P., Arroyo, M., Huerta, A., 2002. Adaptive simulation of the coupled chemo-mechanical concrete degradation. In: Mang, H., Rammerstorfer, F., Eberhardsteiner, J. (Eds.), Proceedings of the Fifth World Congress on Computational Mechanics, WCCM V, Vienna University of Technology, Vienna.

Delagrave, A., Gérard, B., Marchand, J., 1997. Modelling the calcium leaching mechanisms in hydrated cement pastes. In: Scrivener, K., Young, J. (Eds.), Mechanics of Chemical Degradation of Cement-Based Systems. Chapman & Hall, London, pp. 30–37.

Düster, A., Bröker, H., Rank, E., 2001. The *p*-version of the finite element method for three-dimensional curved thin walled structures. International Journal for Numerical Methods in Engineering 52, 673–703.

Fick, A., 1855. Ueber Diffusion. Annalen der Physik und Chemie 94 (1), 59–86.

Gérard, B., 1996. Contribution des couplages mécanique-chimie-transfert dans la tenue a long terme des ouvrages de stockage de déchets radioactifs. Ph.D. thesis, Laboratoire de Méchanique et Technologie, E.N.S. de Cachan.

Gérard, B., 2000. Hydrolysis of cement-based materials: a review. In: Setzer, M. (Ed.), Pore Solution in Hardened Cement Paste. Aedificatio Publishers, Freiburg, pp. 271–304.

Gérard, B., Pijaudier-Cabot, G., La Borderie, C., 1998. Coupled diffusion-damage modelling and the implications on failure due to strain localisation. International Journal of Solids and Structures 35, 4107–4120.

Heukamp, F., Ulm, F.-J., Germaine, J., 2001. Mechanical properties of calcium leached cement paste: triaxial stress states and the influence of pore pressure. Cement and Concrete Research 31, 767–774.

Kuhl, D., submitted for publication. Ion diffusion models based on the Debye–Hückel–Onsager theory applied to calcium leaching of cementitious materials. Journal of Engineering Mechanics.

Kuhl, D., Bangert, F., Meschke, G., in press. Coupled chemo-mechanical deterioration of cementitious materials. Part I: Modeling. International Journal of Solids and Structures.

Kuhl, D., Meschke, G., 2002. Higher order transport models for the simulation of dissociation–diffusion processes in reactive porous media. In: Mang, H., Rammerstorfer, F., Eberhardsteiner, J. (Eds.), Proceedings of the Fifth World Congress on Computational Mechanics, WCCM V, Vienna University of Technology, Vienna.

Kuhl, D., Ramm, E., 1999. Generalized energy-momentum method for non-linear adaptive shell dynamics. Computer Methods in Applied Mechanics and Engineering 178, 343–366.

Le Bellégo, C., Gérard, B., Pijaudier-Cabot, G., 2000. Chemo-mechanical effects in motar beams subjected to water hydrolysis. Journal of Engineering Mechanics 126, 266–272.

Le Bellégo, C., Gérard, B., Pijaudier-Cabot, G., 2001a. Life-time experiments on mortar beams submitted to calcium leaching. In: Ulm, F.-J., Bažant, Z., Wittmann, F. (Eds.), Creep, Shrinkage and Durability Mechanics of Concrete and other Quasi-Brittle Materials. Elsevier Science, Amsterdam, pp. 493–498.

Le Bellégo, C., Gérard, B., Pijaudier-Cabot, G., 2001b. Mechanical analysis of concrete structures submitted to aggressive water attack. In: de Borst, R., Mazar, J., Pijaudier-Cabot, G., van Mier, J. (Eds.), Fracture Mechanics of Concrete Structures. Balkema Publishers, Lisse, pp. 239–246.

Le Bellégo, C., Gérard, B., Pijaudier-Cabot, G., Dubé, J.-F., Molez, L., 2003. Coupled mechanical and chemical damage in calcium leached cementitious structures. Journal of Engineering Mechanics 129 (3), 333–341.

Mainguy, M., Tognazzi, C., Torrenti, J.-M., Adenot, F., 2000. Modelling of leaching in pure cement paste and motar. Cement and Concrete Research 30, 83–90.

Mainguy, M., Ulm, F.-J., 2000. Coupled diffusion–dissolution around a fracture channel: the solute congestion phenomenon. International Journal for Transport in Porous Media 6, 1–19.

Mainguy, M., Ulm, F.-J., Heukamp, F., 2001. Similarity properties of demineralization and degradation of cracked porous materials. International Journal of Solids and Structures 38, 7079–7100.

Newmark, N., 1959. A method of computation for structural dynamics. ASCE Journal of the Engineering Mechanics Division 85, 67–94.

Schwab, C., 1998. P- and Hp-Finite Element Methods. Theory and Applications in Solid and Fluid Mechanics. Oxford Science Publications, Clarendon Press, Oxford.

Simo, J., Ju, J., 1987. Strain- and stress-based continuum damage models. International Journal of Solids and Structures 23, 821–869.

Szabó, B., Babuška, I., 1992. Finite Element Analysis. John Wiley, New York.

Torrenti, J.-M., Mainguy, M., Adenot, F., Tognazzi, C., 1998. Modelling of leaching in concrete. In: de Borst, R., Bićanić, N., Mang, H., Meschke, G. (Eds.), Computational Modelling of Concrete Structures. Balkema, Rotterdam, pp. 559–566.

Zienkiewicz, O., Taylor, R., 2000. The Finite Element Method. Volume 2. Solid Mechanics. Butterworth–Heinemann, Oxford.

Zienkiewicz, O., Xie, Y., 1991. A simple error and adaptive time stepping procedure for dynamic analysis. Earthquake Engineering and Structural Dynamics 20, 871–887.